



# A High-Granularity Digital Tracking Calorimeter Optimized for Proton CT

## OPEN ACCESS

### Edited by:

Vincenzo Patera,  
Sapienza University of Rome, Italy

### Reviewed by:

Chiara Gianoli,  
Ludwig Maximilian University of  
Munich, Germany  
Carlo Civinini,  
INFN, Italy

### \*Correspondence:

Pierluigi Piersimoni  
pierluigi.piersimoni@uib.no;  
pierluigi.piersimoni@gmail.com

### <sup>1</sup>Present address:

TechnipFMC—FMC Technologies  
Measurement Solutions Inc., Norway

### Specialty section:

This article was submitted to Medical  
Physics and Imaging,  
a section of the journal  
Frontiers in Physics

Received: 31 May 2020

Accepted: 16 September 2020

Published: 22 October 2020

### Citation:

Alme J, Barnaföldi GG, Barthel R,  
Borshchov V, Bodova T, van den Brink  
A, Brons S, Chaar M, Eikeland V,  
Feofilov G, Genov G, Grimstad S,  
Grøttvik O, Helstrup H, Herland A,  
Hilde AE, Igolkin S, Keidel R, Kobdaj C,  
van der Kolk N, Listratenko O, Malik  
QW, Mehendale S, Meric I, Nesbø SV,  
Odland OH, Papp G, Peitzmann T,  
Seime Pettersen HE, Piersimoni P,  
Protsenko M, Rehman AU, Richter M,  
Röhrich D, Samnøy AT, Seco J,  
Setterdahl L, Shafiee H, Skjoldal ØJ,  
Solheim E, Songmoolnak A, Sudár A,  
Sølle JR, Tambave G, Tymchuk I,  
Ullaland K, Underdal HA, Varga-  
Köfaragó M, Volz L, Wagner B,  
Widerøe FM, Xiao R, Yang S and  
Yokoyama H (2020) A High-Granularity  
Digital Tracking Calorimeter Optimized  
for Proton CT.  
Front. Phys. 8:568243.  
doi: 10.3389/fphy.2020.568243

Johan Alme<sup>1</sup>, Gergely Gábor Barnaföldi<sup>2</sup>, Rene Barthel<sup>3</sup>, Vyacheslav Borshchov<sup>4</sup>,  
Tea Bodova<sup>1</sup>, Anthony van den Brink<sup>3</sup>, Stephan Brons<sup>5</sup>, Mamdouh Chaar<sup>1</sup>, Viljar Eikeland<sup>1</sup>,  
Grigory Feofilov<sup>6</sup>, Georgi Genov<sup>1</sup>, Silje Grimstad<sup>7</sup>, Ola Grøttvik<sup>1</sup>, Håvard Helstrup<sup>7</sup>,  
Alf Herland<sup>7</sup>, Annar Eivindplass Hilde<sup>7</sup>, Sergey Igolkin<sup>6</sup>, Ralf Keidel<sup>8</sup>, Chinorat Kobdaj<sup>9</sup>,  
Naomi van der Kolk<sup>3</sup>, Oleksandr Listratenko<sup>4</sup>, Qasim Waheed Malik<sup>10</sup>, Shruti Mehendale<sup>1</sup>,  
Ilker Meric<sup>7</sup>, Simon Voigt Nesbø<sup>7</sup>, Odd Harald Odland<sup>1,11</sup>, Gábor Papp<sup>12</sup>,  
Thomas Peitzmann<sup>3</sup>, Helge Egil Seime Pettersen<sup>11</sup>, Pierluigi Piersimoni<sup>1\*</sup>,  
Maksym Protsenko<sup>4</sup>, Attiq Ur Rehman<sup>1</sup>, Matthias Richter<sup>10</sup>, Dieter Röhrich<sup>1</sup>,  
Andreas Tefre Samnøy<sup>1</sup>, Joao Seco<sup>13,14</sup>, Lena Setterdahl<sup>1</sup>, Hesam Shafiee<sup>1,7†</sup>,  
Øistein Jelmert Skjoldal<sup>7</sup>, Emilie Solheim<sup>1</sup>, Arnon Songmoolnak<sup>1,9</sup>, Ákos Sudár<sup>2,15</sup>,  
Jarle Rambo Sølle<sup>7</sup>, Ganesh Tambave<sup>1</sup>, Ihor Tymchuk<sup>4</sup>, Kjetil Ullaland<sup>1</sup>,  
Håkon Andreas Underdal<sup>7</sup>, Monika Varga-Köfaragó<sup>2</sup>, Lennart Volz<sup>13,14</sup>, Boris Wagner<sup>1</sup>,  
Fredrik Mekki Widerøe<sup>1</sup>, RenZheng Xiao<sup>1,16</sup>, Shiming Yang<sup>1</sup>, Hiroki Yokoyama<sup>3</sup>

<sup>1</sup>Department of Physics and Technology, University of Bergen, Bergen, Norway, <sup>2</sup>Wigner Research Centre for Physics, Budapest, Hungary, <sup>3</sup>Institute for Subatomic Physics, Utrecht University/Nikhef, Utrecht, Netherlands, <sup>4</sup>Research and Production Enterprise "LTU", Kharkiv, Ukraine, <sup>5</sup>Heidelberg Ion-Beam Therapy Center (HIT), Heidelberg University Hospital, Heidelberg, Germany, <sup>6</sup>Saint Petersburg State University, St. Petersburg, Russia, <sup>7</sup>Department of Computer Science, Electrical Engineering and Mathematical Sciences, Western Norway University of Applied Sciences, Bergen, Norway, <sup>8</sup>Center for Technology and Transfer, (ZTT), University of Applied Sciences Worms, Worms, Germany, <sup>9</sup>School of Physics, Suranaree University of Technology, Nakhon Ratchasima, Thailand, <sup>10</sup>Department of Physics, University of Oslo, Oslo, Norway, <sup>11</sup>Department of Oncology and Medical Physics, Haukeland University Hospital, Bergen, Norway, <sup>12</sup>Institute for Physics, Eötvös Loránd University, Budapest, Hungary, <sup>13</sup>Department of Biomedical Physics in Radiation Oncology, German Cancer Research Center, Heidelberg, Germany, <sup>14</sup>Department of Physics and Astronomy, Heidelberg University, Heidelberg, Germany, <sup>15</sup>Budapest University of Technology and Economics, Budapest, Hungary, <sup>16</sup>College of Mechanical and Power Engineering, China Three Gorges University, Yichang, China

A typical proton CT (pCT) detector comprises a tracking system, used to measure the proton position before and after the imaged object, and an energy/range detector to measure the residual proton range after crossing the object. The Bergen pCT collaboration was established to design and build a prototype pCT scanner with a high granularity digital tracking calorimeter used as both tracking and energy/range detector. In this work the conceptual design and the layout of the mechanical and electronics implementation, along with Monte Carlo simulations of the new pCT system are reported. The digital tracking calorimeter is a multilayer structure with a lateral aperture of 27 cm × 16.6 cm, made of 41 detector/absorber sandwich layers (calorimeter), with aluminum (3.5 mm) used both as absorber and carrier, and two additional layers used as tracking system (rear trackers) positioned downstream of the imaged object; no tracking upstream the object is included. The rear tracker's structure only differs from the calorimeter layers for the carrier made of ~200 μm carbon fleece and carbon paper (carbon-epoxy sandwich), to minimize scattering. Each sensitive layer consists of 108 ALICE pixel detector (ALPIDE) chip sensors (developed for ALICE, CERN) bonded on a polyimide flex and subsequently bonded to a larger flexible printed circuit board. Beam tests tailored to the pCT operation have been performed using high-energetic (50–220 MeV/u) proton and ion beams at the

Heidelberg Ion-Beam Therapy Center (HIT) in Germany. These tests proved the ALPIDE response independent of occupancy and proportional to the particle energy deposition, making the distinction of different ion tracks possible. The read-out electronics is able to handle enough data to acquire a single 2D image in few seconds making the system fast enough to be used in a clinical environment. For the reconstructed images in the modeled Monte Carlo simulation, the water equivalent path length error is lower than 2 mm, and the relative stopping power accuracy is better than 0.4%. Thanks to its ability to detect different types of radiation and its specific design, the pCT scanner can be employed for additional online applications during the treatment, such as *in-situ* proton range verification.

**Keywords:** proton CT, ALICE pixel detector (ALPIDE), Monte Carlo, hadrontherapy, Complementary Metal Oxide Semiconductor (CMOS)

## INTRODUCTION

Particle therapy, especially with proton beams, has been used and become widely accepted in the last 20 years. The number of dedicated facilities around the world is increasing year by year on a worldwide scale. The most appealing advantage of this technique derives from the physical properties of charged particles crossing matter, which experience a continuous slow down across their path, until they stop and release a large fraction of their initial energy at the end of their range, where the Bragg peak originates. As foreseen by Wilson in 1946 [1] this property allows, in principle, to focus the energy deposition at a certain depth in the human body (e.g., the tumor), sparing nearby tissue and having very low or no exit dose. However, due to the stochastic nature of the particle energy loss, precise calculation of proton range is inevitably uncertain even for simple geometries and materials. For this reason, range uncertainty has become a crucial and still debated topic in proton therapy. On the other hand, even though the precise position of the Bragg peak may be blurred by uncertainty, the considerable clinical benefits of proton therapy is undoubted [2]. To correctly predict the beam range in such a complex geometry as a human body can be, an accurate model of the relative stopping power (RSP, that is, the stopping power of a certain material relative to that of water) of each different material crossed by the particles before reaching the target tumor is needed. Currently, X-ray CT scans are used to image the patient and measure the photon attenuation expressed in Hounsfield unit (HU). Using calibration procedures, HUs for each material are converted to RSP for treatment planning [3]. Together with morphological changes, anatomical deformation due to internal motion, the conversion from HU to RSP is one of the main sources of uncertainty in the range determination, causing errors up to 3.5%, corresponding to up to 4 mm of possible misplacement of the Bragg peak at 10 cm water equivalent range in the patient [4, 5]. Proton CT (pCT) has been acknowledged as having a high potential in reducing uncertainties in proton therapy treatment planning. The strength of pCT is the direct reconstruction of a 3D map of RSP values in the target. The first pCT system idea dates back to 1963, when Cormack proposed protons as probe for CT scans

[6]. The concept of modern pCT scanners is based on the tracking of each single proton history, measuring the direction and position before and after the imaged object and registering the residual energy or range after the object is crossed. Therefore, a typical pCT system must include thin tracking detectors and an energy/range detector. Due to multiple Coulomb scattering the proton track across the target is not a straight line, affecting the spatial resolution of proton imaging. To address this issue, several trajectory estimation methods [7–9] are employed to reconstruct each single proton trajectory using the most likely path (MLP) formalism. Processing the measured particle information by mean of sophisticated image reconstruction algorithms [10–14], a pCT scanner is able to directly yield a 3D map of the RSP values inside the object. Many pCT systems have been proposed and developed in the past 20 years [15, 16] achieving promising results for RSP accuracy and spatial resolution with both Monte Carlo (MC) simulated and experimental setups [17–20]. Lately, the RSP accuracy of pCT was proven to be well below 1% and performs better than modern techniques such as dual energy CT scans [21, 22]. Additionally, pCT has shown reduced noise level and lower dose deposition on the patient with respect to conventional X-ray CT [23, 24]. In recent years, along with protons, heavier ions (mostly helium or carbon) have been considered for imaging given their smaller deviation due to multiple Coulomb scattering. The expected effect of an improved spatial resolution was observed, once the ion fragmentation was taken into account [25–31].

The Bergen pCT collaboration was established at the University of Bergen (Norway) among many institutions across the world<sup>1</sup> with the purpose to design and build a

<sup>1</sup>The members of the Bergen pCT collaboration are: University of Bergen, Norway; Helse Bergen, Norway; Western Norway University of Applied Science, Bergen, Norway; Wigner Research Center for Physics, Budapest, Hungary; DKFZ, Heidelberg, Germany; Saint Petersburg State University, Saint Petersburg, Russia, Germany; Utrecht University, Netherlands; RPE LTU, Kharkiv, Ukraine; Suranaree University of Technology, Nakhon Ratchasima, Thailand; China Three Gorges University, Yichang, China; University of Applied Sciences Worms, Germany; University of Oslo, Norway; Eötvös Loránd University, Budapest, Hungary.

prototype pCT scanner. The aim of the project is to overcome most of the critical limitations of the currently existing prototypes. The most distinctive feature of the prototype design is the employment of a digital tracking calorimeter (DTC), that is, a layer-by-layer pixel detector based on pixelated silicon sensors. Previously, a calorimeter with such features was built and successfully tested with particle beams showing very good performances, despite a number of imperfections, most notably a large fraction of dead or otherwise unusable pixels [32, 33]. Through the participation in the ALICE collaboration at CERN, the Bergen pCT group was able to benchmark the prototype DTC for proof-of-concept for pCT purposes. The idea behind was to use a single technology for both tracking and residual energy measurement in order to simplify the system assembly and to guarantee stable operation in a clinical environment. Using experimental data and MC simulation, proton tracks across the sensor layers were analyzed. A charge diffusion model was applied to estimate the energy deposition by using the size of the charge diffused area and a model fit of the Bragg curve was employed to estimate the residual range, achieving a range resolution of 4% for each proton track. The readout system was able to handle an effective proton frequency of 1 MHz by using 500 concurrent proton tracks in each readout frame uniformly distributed throughout the 16 cm<sup>2</sup> aperture of the detector [34, 35].

In this work an evolution of the described prototype is presented: a novel DTC specifically designed and optimized for pCT, used as both tracking and energy/range detector. This work is then a comprehensive overview of all the multidisciplinary studies necessary to develop the project, which consists in assembling thousands of small silicon detectors together, to form a full scale pCT scanner.

To build such a complex and advanced device, investigations are necessary in order to find solutions to the challenging mechanical and electronic requirements for the successful function of the system. Moreover, the speed of the readout and data processing has to be kept high enough to have a clinically useable instrument. Other aspects to consider are the radiation damage of the instruments, the image reconstruction accuracy, the sensor response when irradiated with a medical beam, just to give some examples. In the following sections, the laborious research work carried out by the Bergen pCT group is described in detail. Nevertheless, to get to the final design, the DTC development was supported by previous studies from the Bergen pCT collaboration.

The new pCT system needs to fulfill the mandatory innovative requirements to handle pencil beams with therapeutic characteristics: high particle rate and localized dose depositions. Therefore, the readout speed has to be fast enough to handle many tracks at the same time and achieve an accurate determination of the ranges of individual protons. The Bergen pCT group has designed both the mechanical and the electronics setup described in detail in the following sections. MC simulations were used to evaluate the potential imaging accuracy of the novel system and the possible damage caused by radiation to the electronic components. Beam tests tailored to the pCT operation with protons and heavier ions have been performed in order to study the cluster size vs. energy deposition in the

epitaxial layer of the sensors and to evaluate the maximum rate (particles per 10  $\mu$ s/frame) the chip can handle.

## MATERIALS AND METHODS

### Design of the Digital Tracking Calorimeter

The segmented DTC has been designed as a multilayer structure made of several detector/absorber sandwich layers, which will function both as tracking system and range/energy detector. The detector will track the traversing particles and assign an energy difference or water equivalent path length (WEPL) to the each single crossing proton and this information will be used in image and CT reconstruction as explained in previous publications [34, 36].

Most pCT scanners currently available utilize a tracking system consisting of two layers of tracking detectors upstream (front tracker) and two more layers downstream (rear tracker) of the object to be imaged. However, in the Bergen pCT scanner, the front tracker has not been included and the information about the impinging proton position and direction will be inferred from the beam optics response of the monitoring system. A system that does not include a front tracker set (denoted *single-sided*, as opposite to the usual pCT scanners with both front and rear tracker planes called *double-sided*) presents some advantages for the design and assembly stages, reducing set-up complexity, final cost, and physical impact on the treatment room. From the operational point of view, a single-sided system would be able to allow a higher particle rate, since the pairing of particle hits measured on the rear tracker with the measurements on the front tracker could be avoided. For a more detailed discussion of this topic please refer to the work of Solie et al. [37].

Although tracking system and energy/range detector form a unique assembly (the DTC), in the next sections they will be described as separate structures and will be referred to as *rear trackers* and *calorimeter*, respectively, in order to better specify the different characteristics.

### The ALICE Pixel Detector Chip

The basic sensor chosen is the ALICE pixel detector (ALPIDE), a monolithic active pixel sensor, initially developed for the upgrade of the inner tracking system of the ALICE experiment at the LHC (CERN) [38]. The ALPIDE is manufactured using the commercial 180 nm Complementary Metal Oxide Semiconductor (CMOS) Imaging Sensor process by Tower Semiconductor. A cross sectional view of the ALPIDE pixel is shown in **Figure 1A**, where the collection diode and the CMOS components are visible. The chip is fabricated on a substrate with a high-resistivity ( $\sim$ k $\Omega$  cm), 25  $\mu$ m thick epitaxial layer. The high resistivity helps to increase the depletion volume of the *pn* junction formed by the collection *n*-well and the *p*-type active volume. The depletion volume can further be increased by applying reverse substrate bias voltage of up to  $-6$  V. The increase in the size of the depletion volume helps in drifting charge to collection diode while reducing charge diffusion. The *n*-wells of CMOS transistors are embedded in additional deep

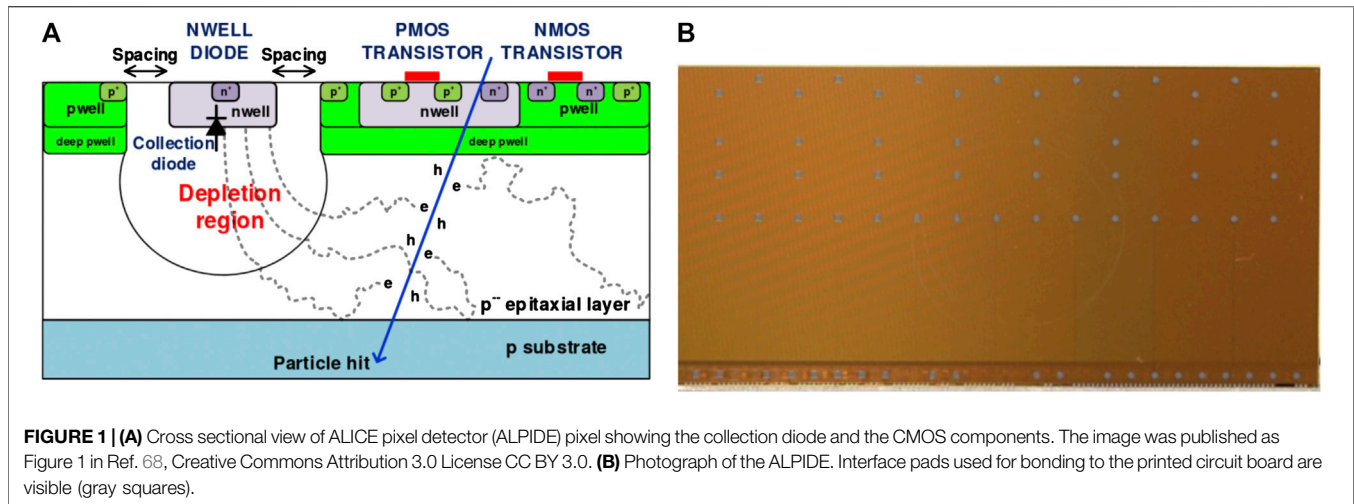


**FIGURE 1 | (A)** Cross sectional view of ALICE pixel detector (ALPIDE) pixel showing the collection diode and the CMOS components. The image was published as Figure 1 in Ref. 68, Creative Commons Attribution 3.0 License CC BY 3.0. **(B)** Photograph of the ALPIDE. Interface pads used for bonding to the printed circuit board are visible (gray squares).

$p$ -wells so that all the charge will be collected only at the  $n$ -well diode. A photograph of a manufactured ALPIDE sensor chip glued to the flexible flat cable is shown in **Figure 1B**.

The chip measures  $30\text{ mm} \times 15\text{ mm}$  and contains a matrix of  $1,024 \times 512$  pixels with in-pixel amplification, shaping, discrimination and multi-event buffering. The pixel size is about  $29\text{ }\mu\text{m} \times 29\text{ }\mu\text{m}$ , which makes the ALPIDE a highly granular sensor capable of simultaneous tracking of multiple particles. The readout of the pixel matrix is hit driven, meaning that the matrix is inactive if there are no hits. The data compression is achieved by implementing a zero-suppression method where data samples of a value smaller than the detection threshold are suppressed. The threshold is applied globally to all the ALPIDE pixels. The S-Curve scan is used to determine the charge threshold and temporal noise of the ALPIDE front-end circuit [39]. The data compression scheme provides efficient detection of particles at high rate. For minimum ionizing charged particles a resolution for the track position measurement of  $5\text{ }\mu\text{m}$ , a detection efficiency of 99.99%, and background probability less than  $10^{-5}$  event/pixel were achieved with ALPIDE [40]. The above-mentioned features make the ALPIDE chip an ideal candidate for the DTC.

## Current Design of the Proton CT System

### Recommended Specifications for the Digital Tracking Calorimeter

The detailed design optimization studies done with MC simulated data by Pettersen et al. [34] focused on different absorber materials and the thickness of the absorber layers. Considering the expectation of the prototype, practical restrictions and MC simulated data, some recommendations were followed, as described below.

- (1) The DTC should have an aperture of  $27\text{ cm} \times 15\text{ cm}$ , to be able to image at least a pediatric head in a single scan.
- (2) In the longitudinal direction, the DTC should be comprised of alternate layers of ALPIDE sensors and aluminum absorber layers. Given that the fraction of

correctly reconstructed tracks and absorber thickness are inversely proportional, the thickness of the absorber should be kept as low as possible, strictly below 4 mm. In this fashion, 41 layers (each made of ALPIDE chips and a support of 3.5 mm-thick aluminum) are required to fully encompass the range of a 230 MeV proton beam and will form the calorimeter. Each layer corresponds to 7.5 mm water equivalent thickness.

- (3) Two more layers will be used as rear trackers. Therefore, they should contain as little material as possible, apart from the sensitive volume of the ALPIDE, in order to reduce the positioning errors due to scattering. This could be achieved by thinning down the support on which the ALPIDEs will be mounted and not including the absorber layer between them.

### The Digital Tracking Calorimeter Prototype

A schematic representation of the DTC is shown in **Figure 2**. The incoming particles will first face the tracking layers, which will have minimum material, as explained above. In **Figure 2**, the support on which the tracker layer will be mounted is not shown, to reveal the arrangement of the sensors in the DTC layers. More explanation can be found in the next section. The sensor layers are stacked in such a way that the transition card (TC) corresponding to alternate layers comes on the opposite side of the main stack, in order to make room for the readout electronics. To fully contain the range of 230 MeV proton beam, 41 aluminum absorber layers will be used, excluding the rear trackers. According to the recommendations made after the design optimization studies, the area of the sensitive part of each layer is designed to be  $27\text{ cm} \times 16.6\text{ cm}$ . Details about distribution of the ALPIDE in these layers is explained in the following sections.

### The Digital Tracking Calorimeter Layers

Each sensitive layer, whether used as a tracker or in the calorimeter, has the same building blocks and design. **Figure 3A** shows the basic structure of half a layer. Each

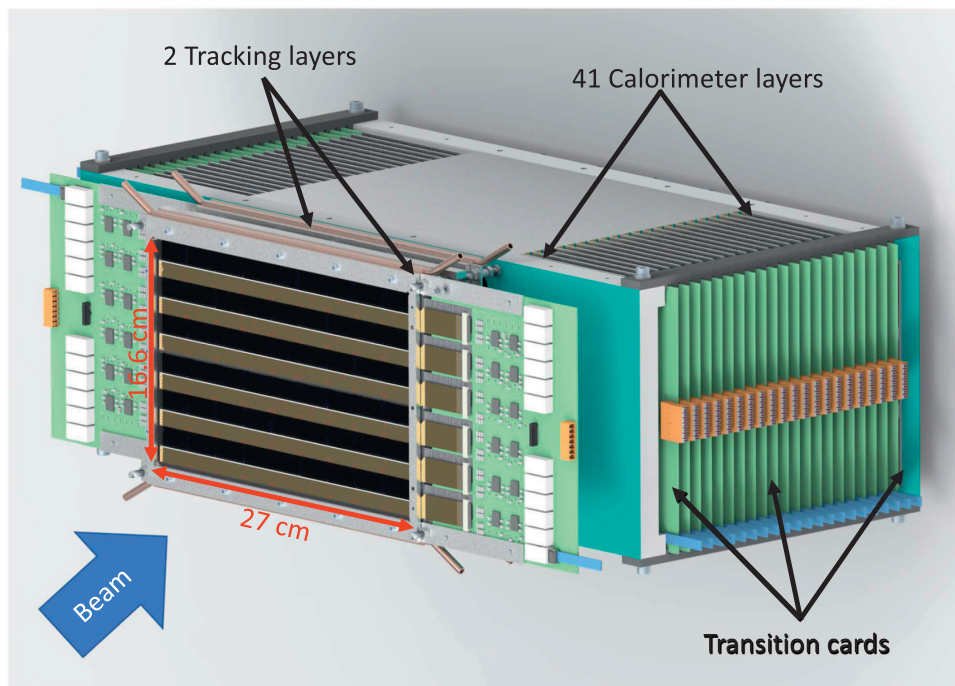


**FIGURE 2** | The general structure of the Bergen pCT system. To reveal the arrangement of the sensors in the layer, the support where the ALICE pixel detector (ALPIDE) sensors will be mounted in the rear trackers is not shown.

ALPIDE chip is mounted on a flex cable, and a collection of nine ALPIDEs mounted on flex cable is called a *string*. Three such strings are then glued to an aluminum carrier (Al 99.5, that is a commercial alloy with aluminum content >99% and a heat conductivity of 220 W/mK, close to that of pure aluminum) of dimension 100 mm × 290 mm × 1 mm called a slab. There are two types of slabs: a top slab (T-slab) and a bottom slab (B-slab). Together they make a half layer, as shown in **Figure 3A**. Although the area of the two aluminum carriers, supporting a top and a bottom slab, is more than the recommended sensitive area of 27 cm × 15 cm, it is not entirely populated by ALPIDE chips, since nearly half of the area is non-sensitive flex cables. Thus, the construction of one layer is achieved by constructing another half layer, with alternated positions of ALPIDEs as compared to the previous half layer. The two halves of the layer are then stacked with the ALPIDEs facing each other and with an air-gap of 2 mm (ensured by an aluminum spacer) between the aluminum carrier boards, as depicted in the side-view schematic of the layer structure in **Figure 3B**.

### Calorimeter Layers

In the calorimeter, the thickness of the absorber layer is chosen to be 3.5 mm. To construct a T- or a B-slab three strings made of 100 μm thick ALPIDE chips will be mounted on a 1 mm thick aluminum carrier board of dimension 100 mm × 290 mm × 1 mm, as described above. To make sure that the two half layers are vertically aligned, they will be screwed to one face of an aluminum absorber plate (Al 99.5) of dimension 200 mm × 290 mm ×

1.5 mm. To assemble a layer, T- and B-slabs are placed on the absorber (chip face up), with both spacers positioned on top of the slabs. After placing a second set of slabs (with chips face down) the whole assembly is fixed by screws. The alignment is done with temporal dowel pins inside the fixing holes. The alternate layers will be rotated around the direction of the beam, to make room for the corresponding readout electronics part. These layers stacked along the beam direction form the calorimeter (**Figure 2**). Units and spacers will be assembled with the help of long screws passing through the aligned holes as shown in the side view of the layer structure in **Figure 3B**. The entire assembly is then supported by an aluminum frame and other support structures. With reference to the side view of the layer structure shown in **Figure 3B**, in the direction of the proton beam, one full calorimeter layer is composed of: the aluminum carriers (1 mm thick), half layer of sensors not facing the proton beam directly, an air gap of 2 mm (ensured by 2 mm thick aluminum spacers), half layer of sensors facing the proton beam, the aluminum carriers on which the sensors are mounted (1 mm thick), and the aluminum absorber plate (1.5 mm thick). In total the calorimeter will comprise 41 of such layers.

### Tracking Layers

In order to minimize the non-sensor material in the tracking layers, 50 μm thick ALPIDE chips will be mounted on ~0.2 mm thick carbon-epoxy sandwich sheets of area 200 mm × 290 mm. These sheets are made of three layers of carbon paper and two layers of carbon fleece and have similar thermal conductivity as that of an aluminum plate of same dimensions. More information

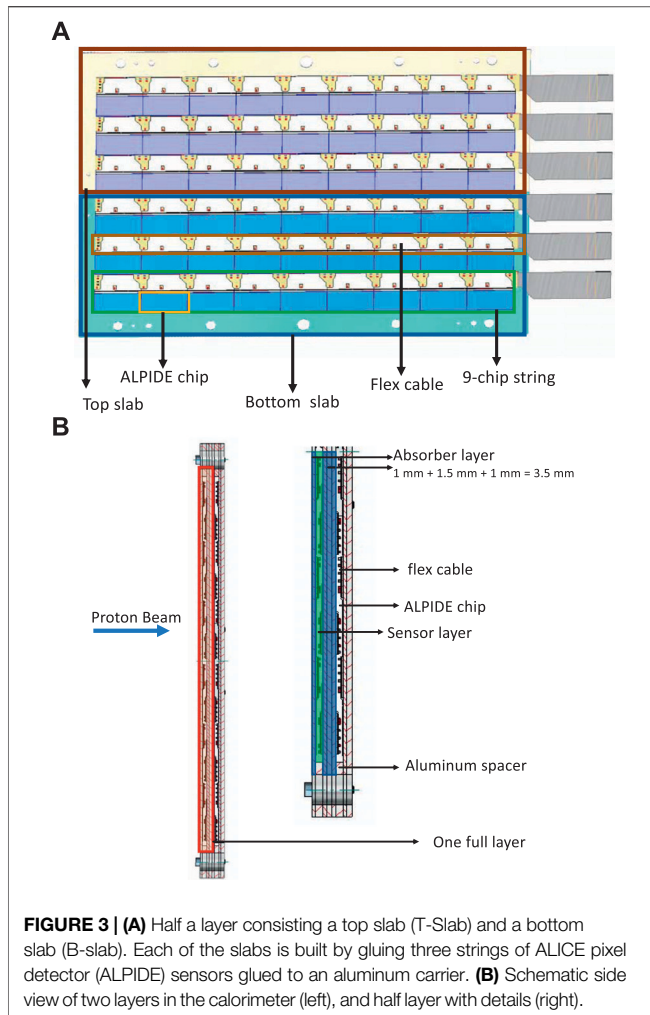


**FIGURE 3 | (A)** Half a layer consisting a top slab (T-Slab) and a bottom slab (B-slab). Each of the slabs is built by gluing three strings of ALICE pixel detector (ALPIDE) sensors glued to an aluminum carrier. **(B)** Schematic side view of two layers in the calorimeter (left), and half layer with details (right).

about this material can be found in Refs. 41 and 42. The arrangement of the ALPIDE chips in a half layer will be the same as shown in **Figure 3A**, except that a single carbon-epoxy slab supported by an aluminum frame will carry the chips. This

makes the half layer more stable and easier to handle with respect to the layers in the calorimeter made of two half slabs. Two half layers, with chips facing each other, are then clamped together with 2 mm thick aluminum spacers sandwiched between them at the top and bottom. Analogous to the calorimeter layer, in the direction of the proton beam, one full tracker layer is composed of: a carbon-epoxy sandwich sheet (0.2 mm thick) with half layer of sensors not facing the proton beam directly, an air gap of 2 mm, a half layer of sensors facing the proton beam, and a carbon-epoxy sandwich sheet. The half layer of sensors is 0.2 mm thick. The second layer will be constructed exactly in the same way and placed at a distance 50 mm in accordance with literature [43].

### Cooling of the Digital Tracking Calorimeter

For the most common operating conditions of a pCT scan, the power consumption by each chip is estimated to be 202 mW, corresponding to ~900 W for the full DTC. This estimation is based on the work of Šuljić et al. [44]. Other parts of the detector such as TCs and readout electronics also require cooling. The cooling mechanisms of each separate part of the detector, according to the requirement for each component, is described below.

#### Calorimeter Layers

The temperature distribution in the calorimeter layers was investigated based on the simplified geometry shown in **Figure 4**. The half layers are well isolated from each other by air gaps. The thermal resistances of chips, cables, glue, absorbers, and carrier plates perpendicular to the layers are negligible, thus a two-dimensional temperature distribution was considered. To study the steady state temperature distribution, load and geometry were assumed to be homogeneous across the string, so the temperature of a point just depends on its longitudinal coordinate. The heat transfer was studied in the absorber and carrier plates only. The detailed calculations can be found in Ref. 45. The liquid cooling system will likely use water as a coolant and each layer temperature will be monitored by temperature sensors.

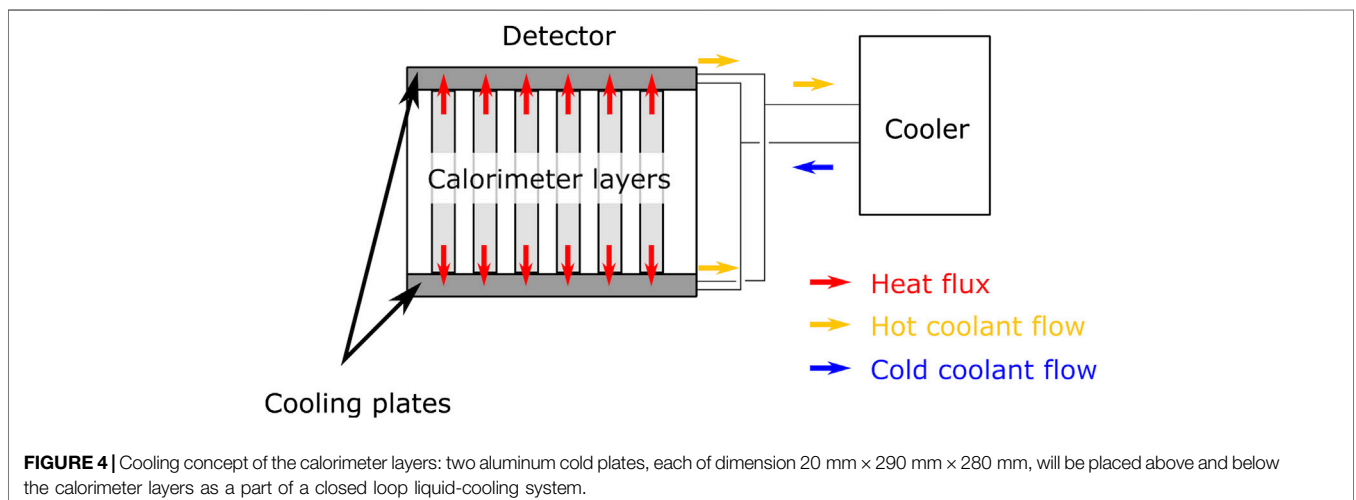
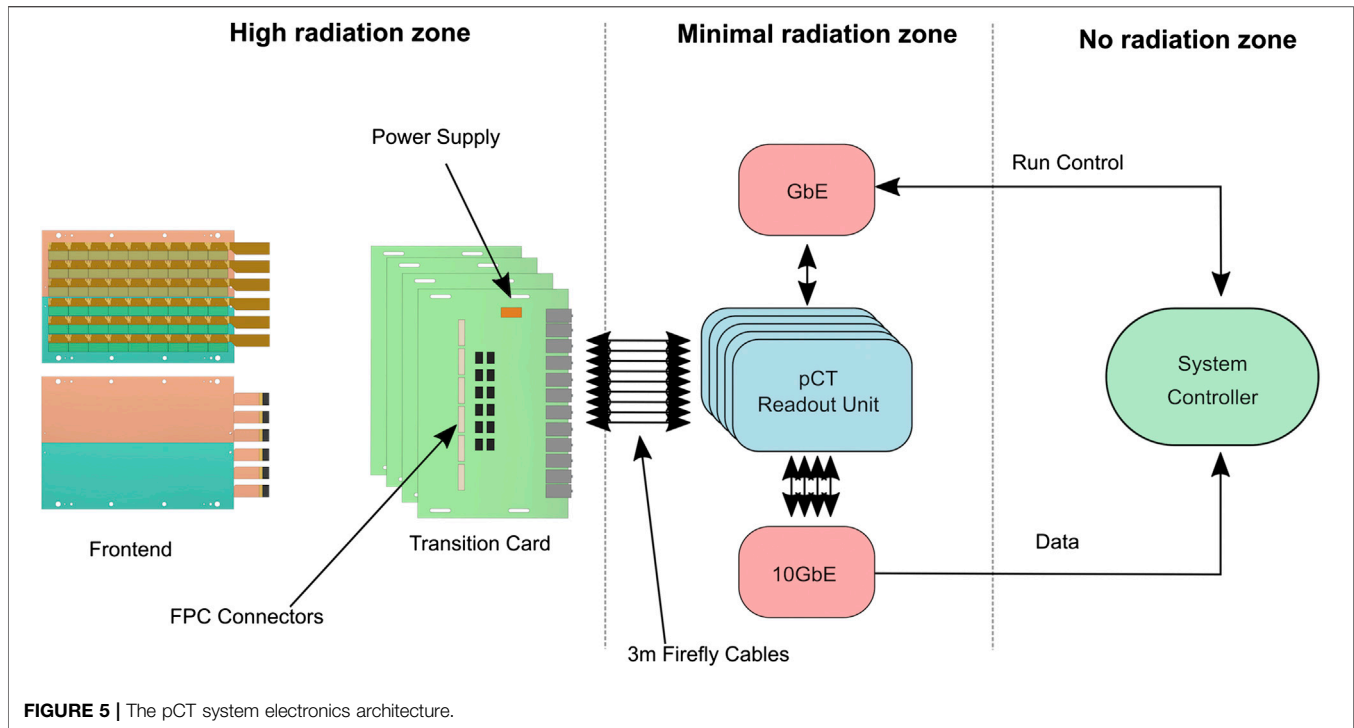


**FIGURE 4 |** Cooling concept of the calorimeter layers: two aluminum cold plates, each of dimension 20 mm × 290 mm × 280 mm, will be placed above and below the calorimeter layers as a part of a closed loop liquid-cooling system.



### Tracker Layers

In the tracker layers, the chips will be mounted on very thin carbon-epoxy sandwich sheets with similar heat draining capacity as that of an aluminum sheet of the same dimension, which may pose challenges for cooling. Hence, a combination of air and liquid cooling will be used to cool these layers. As depicted in **Figure 2**, the aluminum support frames around the carbon-epoxy sandwich sheets are fitted with water cooling on the top and bottom edges. In addition, an airflow around the carbon-epoxy sandwich sheets will be used to cool the chips. Parts of the air-cooling system are not shown in **Figure 2**.

### Transition Cards

The TCs will be monitored by a temperature sensor mounted on each one of them, and they will be cooled by forced air.

## The Digital Tracking Calorimeter Electronics Conceptual Design

The pCT data acquisition (DAQ) and run-control system consists of three distinct parts: 1) the frontend electronics, 2) the TC, and 3) the pCT readout unit (pRU). In **Figure 5** a schematic of the Bergen pCT system electronics architecture is shown.

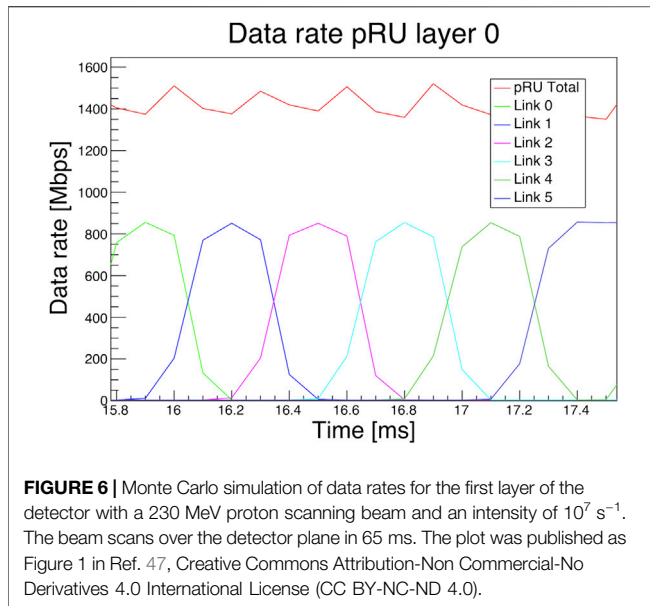
The DAQ and run-control system were designed to satisfy the requirements described below.

- (1) Radiation must not damage nor critically interfere with the operation of the detector. As shown in **Figure 5**, the first two components are placed in a high-radiation area, while the pRUs

are placed in an area with much less ionization fluence, at least 2 m from the detector center. This reduces the particle fluence and relaxes the requirements for radiation mitigation techniques employed on the pRU. MC simulations (described in *Simulated Radiation Damage*) of the radiation environment with a beam intensity of  $10^7 \text{ s}^{-1}$  shows that for all the FPGAs of the system, one can expect a single event upset (SEU) every 2,933 s. This is within an acceptable rate and can be handled with simple off-the-shelf mitigation techniques.

- (2) The system is capable to interface  $108 \times 43$  pixel sensors with both slow control and high-speed data capture. Careful considerations were taken into account both on the frontend electronics design, the TC, and the pRU to minimize noise and errors.
- (3) Clock and trigger signals must be deterministically distributed to all the sensor chips.
- (4) The system must be able to handle the data stream generated by a  $5 \mu\text{s}$  frame time and a proton beam intensity of at least  $10^7 \text{ s}^{-1}$ . The  $5 \mu\text{s}$  frame time represents a lowest limit which should never be reached in a real case scenario. System C-simulations [46] with these numbers gave a data rate of roughly 1.4 Gbit/s for each layer [47], as shown in **Figure 6**. The simulation of data rates for the first layer of detector was performed with a 230 MeV proton scanning beam and an intensity of  $10^7 \text{ s}^{-1}$ . The pRU firmware is designed to deal with up to seven times these data rates.

The system is based on a trigger-less readout architecture, i.e., no external nor any high-level trigger system is implemented. However, a continuous sequence of pulses from the readout electronics is used to initiate data frames on the sensors. All



pixels firing within the time frame are stored in a snapshot of data. The frame duration is set to be shorter than the pulse interval, typically slightly less than  $10 \mu\text{s}$ . The gap between each frame is at minimal 25 ns, but it can be optimized in the future to avoid a lot of so-called double hits (that is a particle's signal detected within two separate frames). The frame frequency, frame duration, and gap are customizable, but always constant for a given run. When the final time between each 2D projection is known, this time is used to create trains of continuous pulses, i.e., several sequences of pulses, with longer pause between each sequence.

### Frontend Electronics

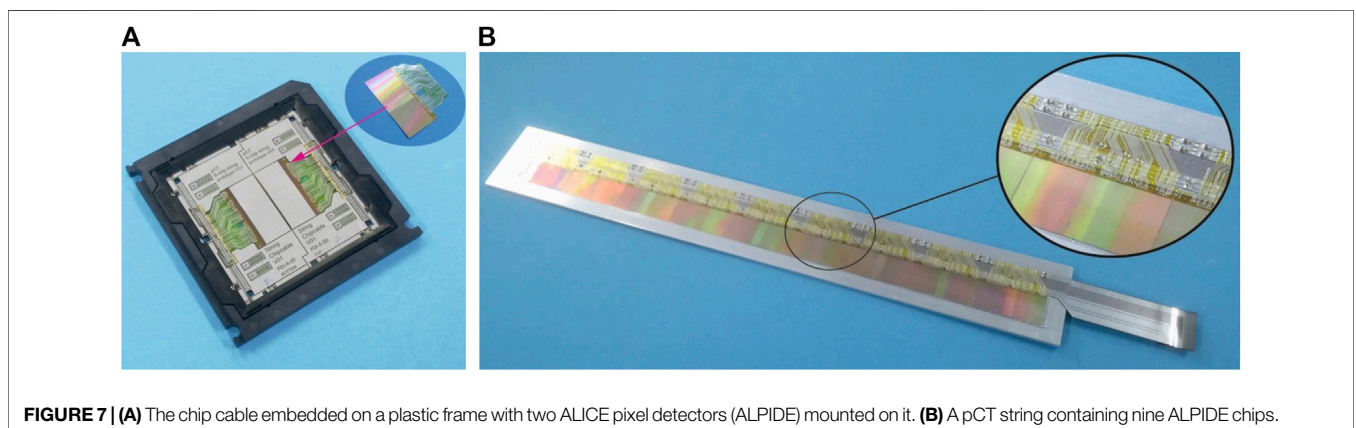
Each detector layer is electrically identical and is composed of 108 ALPIDE chip sensors. Nine chips are mounted together on a string where clock and slow control signals are shared. The chips are configured in high-speed data mode, and each chip has its own 1.2 Gbit/s low-voltage differential signaling (LVDS) data link. No signal multiplexing is possible because of the

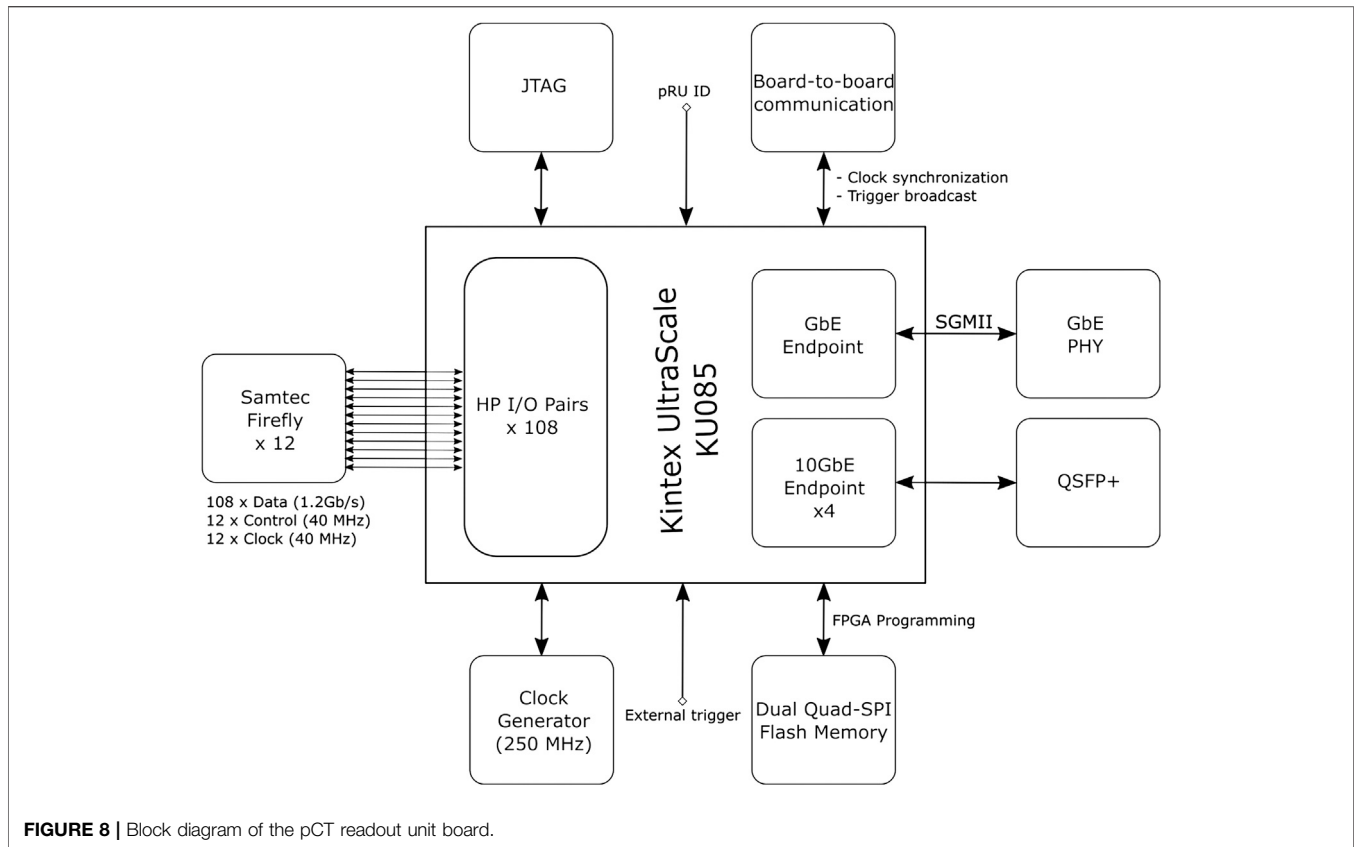
periodically high data rates. As described in The DTC Layers, a full layer is constructed by having two half-layers facing each other. This causes an air gap of about 2 mm inside a layer, providing room for critical decoupling capacitors. The ALPIDEs are bonded to thin, flexible printed circuits (FPCs) of aluminum and polyimide called chip cables or flex. Single-point Tape-Automated Bonding is chosen instead of traditional wire-bonding to increase reliability [48]. The chip cables are bonded with the same method to longer FPCs in the size of the string, providing the electrical connection outside of the detector area. Using chip cables for connecting the ALPIDEs to multilayered longer FPCs allows to perform ALPIDE functional testing after Single-point Tape-Automated Bonding and exclude mounting defective chips in the strings. Such an approach allows the increase of reliability and production yield at assembling string and DTC as a whole. Several iterations of chip cables and string FPCs have been produced and tested. In the final version (**Figure 7A**), the chip cables are bonded to the  $88 \mu\text{m}$  pads on the side of the ALPIDE chips. Testing the prototype of the string (**Figure 7B**) has shown that this method provides the best results in terms of jitter and noise on the high-speed links.

TC is used as an intermediate medium between the frontend electronics and the readout electronics for each layer. These cards also deliver stable power to the sensors. Six FPC connectors are mounted on each side of the printed circuit board providing both power and signaling connectivity to the sensors. As the TC is placed in a high-radiation area, only pre-tested radiation tolerant components are used for power regulation. Twelve Samtec FireFly connectors are used to transmit data from the TC, and control and clock signals from the readout electronics.

### Readout Electronics

The pRU is under development but is clearly defined based on testing with the Xilinx VCU118 Evaluation Kit. The pRU is based on a Xilinx Kintex Ultrascale FPGA. The FPGA's native I/O primitives provide high enough bandwidth to handle the 108 data links without employing multi-gigabit transceiver pins reducing the need for a larger and more expensive FPGA [47]. **Figure 8** shows the functional block diagram of the pRU. The FireFly connectors are connected to the High-





Performance (HP) I/O banks of the FPGA. A single I/O bank handles 24 LVDS pairs, so a total of 4.5 I/O banks are used for this purpose, less than 50% of the total available pins. Simple Gigabit Ethernet for run control is provided using IPBus protocol [49], and up to four separate 10 Gbit Ethernet links are provided to handle the data offload. A custom protocol is implemented to obtain a safe high-speed data transmission over user datagram protocol (UDP). The pRUs are placed together in a crate that supplies power and allows for board-to-board communication and synchronization.

### Data Processing and Track Reconstruction Readout Performances

During the prototype phase, the focus for the readout software is to provide small and scalable tools. An upper limit of the expected data rate is used to estimate the size of the system. The short acquisition time of approximately 1 s allows to store all data on host machines and run most of the raw data processing without intermediate or permanent storage. The pRU is supporting up to four independent 10 Gbit links for the data offload, giving a maximum amount of data of 5–10 GB per layer for a 1–2 s acquisition window. This is an upper limit; the actual data rate depends on beam conditions and the position of the layer in the setup. As illustrated in **Figure 6**, the data rate for the first layer with a realistic beam intensity will be much lower than the upper estimate. The total amount of data for an acquisition window of

1 s will be approximately 10 GB. The readout software is designed as a collection of smaller applications communicating via message queues and shared memory. These software components run independently and in parallel and can be distributed as multiple instances on several host machines. Following this variable approach, the readout system can be scaled according to the needs. The main part of the readout software is a client application connecting to servers running on the pRU hardware. Data between pRU and the client(s) are transferred using UDP network protocol. A dedicated transport format on top of UDP, the pCT Data Transport Protocol (pDTP), has been defined to ensure a reliable communication between clients and servers. Accordingly, the client application is named pDTPClient. The pDTPClient stores data in shared memory regions of the host machines and announces them to the subsequent processors. Preliminary measurements for the raw transport between pRU and host machine have been presented in Grøttvik et al. [47]. For further processing, reconstruction, and storage of data, the pRU data is handled by a parser/decoder application which unpacks and sorts ALPIDE chip data as prerequisite for further processing and monitoring of the data. For the prototype phase the collection of individual applications will be used together with scripts and command line interface.

The readout speed of the DTC can be easily adapted to the beam facility where it is operated. It can handle either spill-operated or quasi-continuous beams at synchrotron or cyclotron facilities, respectively. In any case, the estimated dataset size for a 2D

projection is limited to 400–800 GB transmitted over 1–2 s. The regular dataset size is expected to be below 400 GB over 2 s, so, as first estimate, 200 Gbit/s uplink and 20 GB/s disk write speed should be sufficient. Until first realistic full experimental runs are taking place, it is not clear how much bandwidth and latency is needed. Therefore, the system is laid out for scalability on each level. Each readout card has a Quad Small Form-factor Pluggable (QSFP+) connector that is capable of outputting 40 Gbit/s. It will be connected by 5 m copper cables ending in four 10 Gbit/s connectors on a regular 48-port ethernet switch. These switches usually have several fast uplink ports. The switch will be connected by at least two 100 Gbit/s uplinks to the DAQ computer(s). The data will be transferred first into RAM that acts as a burst buffer before writing to disk. A modern single non-volatile memory Express solid state disk, that is connected via peripheral component interconnect Express 4, can have a write performance of up to 6.5 GB/s, so a redundant array of independent disks of those solid state disks should achieve the necessary write speed of 20 GB/s. The data will be moved to a large capacity storage to free the fast redundant array of independent disks for the next measurements. Each readout card should take care of several detector layers, the exact number can be adjusted to the hit density of different layers. Current Ethernet switches can provide up to 400 Gbit/s per socket, although not with copper cables, so the few uplink cables might be optical. This will be also beneficial for a more flexible positioning of the computers. It is also possible to add more switches, if the internal bandwidth is not sufficient. Additional network interface cards with hardware offload capacity can be added. Since the data has a timestamp, the output stream can be segmented and saved on several DAQ computers to avoid bottlenecks and to be combined in a later step.

### Track Reconstruction in the Digital Tracking Calorimeter

Thanks to the segmented structure of the DTC, it is possible to track proton histories crossing the several layers. In an experimental run, a high multiplicity of proton tracks will be recorded in each readout cycle in order to increase the proton rate above the electronics frame acquisition rate of  $\sim 10 \mu\text{s}^{-1}$ . The resulting data output will consist of pixel-clusters centered around each of the 50–100 proton tracks contained in a single readout. An extrapolating track-following algorithm will trace the estimated path of each proton, starting from the clusters in the distal layers of the detector [50]. A track is considered correctly reconstructed when it contains both the endpoints of the true track. Using a track scoring and track splitting model described in previous publications [36, 51], between 75 and 95% of the tracks can be correctly reconstructed, depending on object thickness, multiplicity and pencil beam size. The remaining are predominantly pairwise confused close tracks, mainly in the Gaussian core of the pencil beam, due to multiple and high angle scattering. Their effect on the reconstructed images has not been quantified but is expected to be minor due to the  $3\sigma$  filters applied during image reconstruction. The  $dE/dz$  curve of each track can be then calculated from the sizes of the clusters along the track and a Bragg-Kleeman depth dose curve will be used for precise range fitting, for rejection of nuclear events, and for particle identification in the case of ion imaging, leading to a

sub-millimeter systematic range resolution for object sizes ranging between 0 and 300 mm WEPL [36].

## Expected Digital Tracking Calorimeter Performances: Experimental and Simulated Investigations

### Experimental Setups

The ALPIDE chips were tested by the Bergen pCT collaboration to evaluate the response to different sources of radiation. Using an  $^{241}\text{Am}$  source the cluster evolution within the epitaxial layer could be studied. A cluster is defined as the collection of neighboring pixels that fires within the same time frame. When a particle traverses the epitaxial layer of the ALPIDE it deposits charge, which can be collected by the individual collection diodes of the pixels. A pixel records a hit and stores it in one of the three in-pixel memory banks, if the signal from the analog front-end surpasses the threshold limit. The evolution of a cluster could be observed by using a sufficiently fast data frame rate.

To identify clusters in the readout frames, an algorithm was used that isolates one frame and loops through the pixel matrix ( $1,024 \times 512$ ) until it finds a hit. It then proceeds to find the nearest neighbor. If this is adjacent to the selected pixel the cluster size increases. If the nearest neighbor is not adjacent or there are no more hits in the selected frame, the cluster size is stored, and the size of the next cluster is calculated.

The cluster size distribution of low and high occupancy environments was studied to verify that the charge collection process in the analog front-end of the ALPIDE is independent of occupancy. Ideally, a low occupancy run consists in setting a particle rate low enough to have single clusters per frame, compared to high occupancy when many clusters in the same frame are collected. This is not always possible with a real beam at medical facilities, so the low occupancy was studied with a particle rate as low as possible (15 kHz) and the high occupancy with a 10 times higher rate (145 kHz).

The experimental data presented in this work were acquired at the Heidelberg Ion Therapy (HIT) facility, Heidelberg, Germany in two different experiments in July and December 2018. Proton, helium, and carbon ions were used to irradiate the ALPIDE chips. For the experiment of July 2018, a telescope detector composed of three different ALPIDEs was assembled and installed at the HIT facility. For the helium beam five different energies were tested: 220.5, 200.38, 150.11, 100.19, and 50.57 MeV/u, corresponding to a FWHM at the isocenter of 10.1, 10.2, 11.1, 12.9, and 20.6 mm, respectively. For the proton beam three energies were tested: 221.06, 200.11, and 48.12 MeV, corresponding to 12.6, 12.8, and 32.7 mm FWHM at the isocenter, respectively. The extraction time for the beam was 12 s. The data frame rate was set at 100 kHz, with a frame duration of  $9.750 \mu\text{s}$ . The intensity of the beam was approximately 100 kHz. For the experiment of December 2018, in addition to proton and helium ions, also carbon ion beams were used for irradiation. The ALPIDE chips were glued to a flex cable similar to the one that will be used for the final prototype. The energies used were 48.12 MeV for protons, 50.50 MeV/u for helium, and 88.83 MeV/u for carbon. Additionally, plastic degraders [made of polymethyl methacrylate (PMMA)] were

used in order to have different sections of the Bragg curve (from plateau to peak) on the ALPIDE chip, so that the different response of the chips could be studied. The beam intensity and extraction time were the same as for the July experiment. The back bias was set to 0 V for both the experiments.

## Simulated Imaging with the Digital Tracking Calorimeter

### Simulation Setup

The MC framework GATE version 8.2 [52, 53] with Geant4 version 10.5.1 [54, 55] was used to build an accurate representation (described below) of the DTC sandwich structure in terms of slabs that account for the full material budget of the DTC. This model was used to simulate and reconstruct proton radiographs (pRad) and full pCT scans with different phantoms, as explained below. The physics builder list QBBC\_EMZ was activated for the simulations, as recommended by the GATE Radiation Therapy and Dosimetry working group. The simulation world was filled with air with default step limits and production cuts. The step length inside the DTC was limited by the small slab thicknesses and production thresholds for  $\gamma$ ,  $e^\pm$  and protons were set to approximately half the slab thickness in the respective geometries inside the DTC. The mean ionization potential of water was set to 78 eV. The beam characteristics at the beam window position placed 500 mm before the isocenter are reproduced from **Table 1** in the work by Sølief et al. [37]. A total of 5,000 protons per beam spot was kept consistent across all simulations to ensure sufficient statistics and approximate the expected protons intensity of  $10^7$  protons per second in a realistic scenario.

### Modeling of the Digital Tracking Calorimeter

The MC implemented DTC is a model of the system described in the previous sections. The MC model used in this work had exactly the same materials and material budget as the planned detector, except that all the detector components were approximated as slabs with different thicknesses to eliminate the intended overlapping structures and subsequent calibration. These components included support plates functioning as carriers and energy absorbers (carbon-epoxy sheets for the trackers, aluminum for the calorimeter), epoxy glue, ALPIDE and accompanying flex cables. The flex cables were simulated as three Al/polyimide foiled dielectric components (chip-cable, top, and bottom) and a Kapton spacer. No casings or structural supports surrounding the outside of the detector were included in the simulations since these have no impact on the proton interactions, tracking, and final energy reconstruction. The simulation reproduced the same structures of 43 ALPIDE/carrier sandwich layers described above. The layers in the calorimeter were simulated as the assembly of 3.5 mm thick aluminum plates spaced 2 mm apart, two slabs of silicon representing the ALPIDE, flex cables, and glue. This structure was repeated a total of 41 times, amounting to a length of 225.5 mm. As for the real DTC, the rear trackers differ from the calorimeter layers for the carriers made of carbon-epoxy sheets instead of aluminum, and a thinner ALPIDE chip. The total volume of the simulated DTC was 270.0 mm  $\times$  165.0 mm  $\times$  225.5 mm. In **Figure 9** a representation of the MC modeled

detector with details of the slab thicknesses and materials is shown.

The distance between the first plane of the tracker pair to the phantom edge was set to 150 mm and the distance between tracking planes in each set was 50 mm based on the results from Bopp et al. [43] and Krah et al. [56].

### Simulated Proton Radiographs and Proton CT

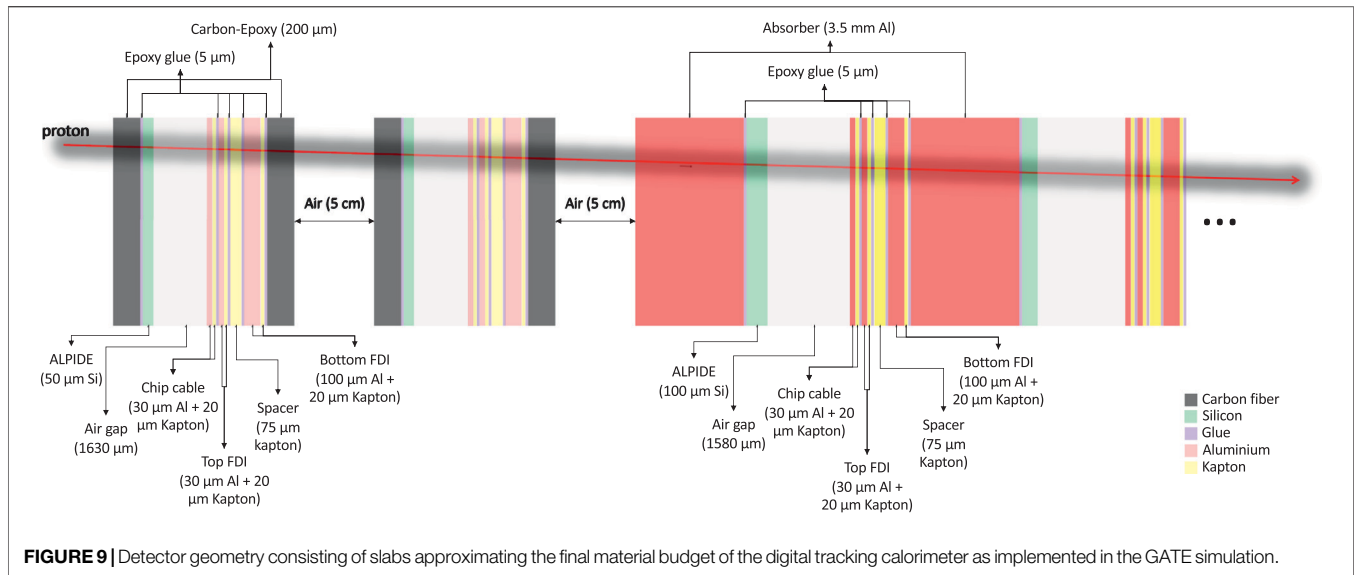
To give an estimate of the performance of the final DTC prototype, reconstructed images from GATE simulations are presented. The simulation considers a detailed model of the final tracking layers of the DTC as described in the previous section. The accuracy and precision of the reconstructed WEPL information achieved with the DTC was modeled following the detailed investigation on the systematic and stochastic uncertainty presented in the work of Pettersen et al. [36], repeating the analysis for the final 3.5 mm aluminum absorbers chosen for the DTC. The modeling was performed as a two-step process. First, the residual energy of the protons was determined from an ideal energy scorer placed right before the first tracking layer and converted to WEPL by integrating the inverse stopping power in water from initial to residual energy. The necessary stopping power table was obtained from the Geant4 code underlying the GATE simulations directly, by calculating the stopping power in water at steps of 0.01 MeV using the GetTotalDEDX function of the G4EmCalculator class. Second, to model the detector response in simulations, for each proton, the WEPL obtained from the MC simulation, calculated from the difference between the initial and outgoing energy, is shifted by the systematic uncertainty inherent to the detector response. Then, this WEPL is blurred-out by sampling from a Gaussian distribution with standard deviation given by the range straggling in the detector. These detector responses are characterized by the work done by Pettersen et al. [36] and applied to the MC model of the detector presented above. This is henceforth called the *modeled* setup.

For the sake of comparison, an ideal pCT system (no material budget in the trackers and exact energy measurement of incoming and outgoing energy) was simulated to be compared to the modeled DTC. A realistic proton therapy beam line was modeled utilizing the GATE pencil beam scanning [57]. The pencil beam lateral FWHM was set to 7 mm, with an angular divergence of 2.5 mrad and emittance of 3.0 mrad mm. An equal number of particles was used in each pencil beam spot, and the lateral distance between spots was set to 7 mm. The distance between source and isocenter was 500 mm.

### Simulated Phantoms

Two different phantom geometries were implemented as described below.

- To assess the achievable RSP accuracy of the system the Catphan® (The Phantom Laboratory, Salem, NY, United States) CTP404 module (henceforth called *CTP404 phantom*) was used. The phantom is made of an epoxy



cylinder of 40 mm height, and 150 mm diameter, and contains eight cylindrical cavities of 12.2 mm diameter, six of which are filled with different plastic inserts, and 2 with air. For material and compositions please refer to Table I in Piersimoni et al. [30]. RSP values for each material were calculated from MC simulations and are: 1.363 (Delrin), 1.179 (PMMA), 1.048 (Polystyrene), 1.003 (LDPE), 0.886 (PMP), 1.833 (Teflon), and 1.143 (Epoxy).

- For a clinically relevant case, a digitized pediatric head phantom based on the CIRS model HN715 (Norfolk, VA, United States) was simulated. The head is a high resolution ( $0.1875 \text{ mm} \times 0.1875 \text{ mm} \times 1.25 \text{ mm}$ ) voxelized geometry implemented by Giacometti et al. [18]. The phantom comprises different human tissue materials ranging from brain to tooth enamel. A detailed tissue composition can be found in Sølief et al. [37].

The phantoms were placed such that their rotational center coincided with the isocenter of the pencil beam scanning system. The distance between the phantom edge and the first tracking layer of the DTC was 150 mm.

### Image Acquisition

Full pCT scans of both phantoms were acquired in a step-and-shoot technique from 360 projections separated by  $1^\circ$  angular steps. This reflects the future application of the prototype, as the necessity to rely on a scanned beam for list-mode particle imaging (tracking each single particle crossing the object) without front trackers makes a continuous scan acquisition infeasible. Each projection contained  $3.5 \times 10^6$  protons at initial energy of 230 MeV. A total of  $1.3 \times 10^8$  protons entered the reconstruction volume of the CTP404 phantom module, and  $7.9 \times 10^8$  protons entered the reconstruction volume of the head phantom. In addition, a proton radiograph was acquired of the head phantom, for which  $10^7$  primary protons at 230 MeV initial energy were used.

### Image Reconstruction

Before image reconstruction a  $2.5\sigma$ -filter on the proton angles was applied to filter out the large angle scattering not described by the scattering theory underlying the MLP [8]. Similarly, during the reconstruction, a  $3\sigma$ -filter is applied to the WEPL distribution in order to remove unusually large energy losses and nuclear interactions [24]. Since the modeled WEPL does not consider the additional nuclear interactions that protons may undergo in the DTC, a  $3\sigma$ -WEPL filter is sufficient to ensure high quality images [58]. For the final prototype, additional data filters will act on the track reconstruction, measured cluster sizes and the Bragg-peak fitting performed [64].

To minimize the error in the proton path estimation associated to the absence of the front tracker, the extended MLP formalism developed by Krahe et al. [56] was employed, with some modifications adopted to speed up the reconstruction time, as explained below. This formalism enables MLP estimation in a single-sided setup utilizing the known parameters from the pencil beam scanning system (spot positions, lateral and angular uncertainty, as well as lateral/angular covariance). The necessary beam parameters were obtained at the same distance to the phantom as would be the innermost front tracker plane in a double-sided system.

Radiographic images were produced using the maximum likelihood image reconstruction method developed by Collins-Fekete et al. [59]. For pCT reconstructions the diagonally-relaxed orthogonal row projection iterative reconstruction algorithm with total variation superiorization was used [12]. An analytical Feldkamp-David-Kress CT reconstruction based on rear tracker binning produced the starting point for the iterative algebraic reconstruction. For computational efficiency, only the entrance and exit position/direction of each proton were calculated from the extended MLP formalism, while the extended MLP using a MLP-cubic spline path (CSP) [60] hybrid was approximated. For this hybrid, first the optimized entrance and exit position/direction vectors are calculated from the extended MLP,

then these optimized position/direction vectors are used as input to a CSP estimate. The CSP estimate results faster than the MLP as a consequence of fewer floating-point operations to be performed at each depth. Although this approximates the performance of the full extended MLP formalism, it retains the runtime benefit of the CSP algorithm. The slice thickness was set to 1.25 mm for both the phantoms, and  $455 \times 455$  pixels per slice (0.35 mm pixel size) and  $240 \times 240$  pixels per slice (0.75 mm pixel size) were set for the reconstruction of the CTP404 and pediatric head phantom, respectively. The data were divided into 40 optimization blocks per iteration and the algorithm was stopped after eight iterations. The reconstruction parameters were kept the same as in previous studies [18, 19, 30, 31] investigating the same phantoms with different detector designs, such that a direct comparison between different pCT systems is possible. Optimization of the parameter settings for the single-sided design was out of the scope of this work.

### Simulated Radiation Damage

To perform a pCT scan, DTC and readout electronics need to be placed directly in the path of the proton beam exiting a patient. In a potential clinical setting, the DTC will also likely be fixed onto a rotating gantry and be present during proton therapy. A relatively large amount of radiation is therefore expected to hit radiation sensitive readout electronics. Inside a proton therapy treatment room where energetic hadrons are present, SEUs are expected to be the main radiation damage effect as the SRAM based FPGAs used in the pRU are particularly prone to experiencing them. SEUs are induced by single particle hits that are energetic enough to cause a change in the data state of a memory cell in the FPGA (a bit flip) and it is one of the main concerns for the pRU [61]. Other damaging effects affecting the potential lifetime of electronics include the total ionizing dose (TID) and non-ionizing energy loss (NIEL). The FLUKA MC code [62, 63] offers explicit scoring of relevant particles, called “hadrons with energy greater than 20 MeV” (HADGT20M) affecting the rate of SEU, and “fluence of Silicon 1 MeV-neutron equivalent” particles scaling with NIEL. The HADGT20M and Silicon 1 MeV-neutron equivalent fluence inside and surrounding the DTC was investigated using FLUKA version 2011-3.0 in combination with Flair version 3.0-10.

A general pCT setting consisting of 230 MeV scanned proton beams passing through a cylindrical water phantom (height 20 cm and radius 8 cm), and a separate proton therapy setting forming a 5 cm wide spread out Bragg peak (proton energies 77–116 MeV) covering a  $5 \text{ cm} \times 5 \text{ cm} \times 5 \text{ cm}$  target volume in the center of the cylindrical water phantom were tested. In these FLUKA studies, the maximum dose deposited on the ALPIDEs composing the DTC, and in six separate FPGA objects located at increasing lateral distance (10, 50, 100, 200, 300, and 400 cm) away from the DTC was evaluated.

The radiation environment formed by the two relevant particle fluences, and the deposited dose were normalized to an assumed intensity of  $10^7$  protons per second for pCT, and  $3.11 \times 10^8$  protons per second in proton therapy. The proton intensity in proton therapy was based on an average treatment

fraction delivering a physical dose of 2 Gy inside the target volume in 100 s.

The FPGA health in terms of number of SEU can be approximated by:

$$N_{SEU} = \sigma_{SEU} \times \Phi_{HEH} \times N_B, \quad (1)$$

where  $\sigma_{SEU}$  is the SEU cross section of the FPGA,  $\Phi_{HEH}$  is the fluence of  $>20$  MeV hadrons, and  $N_B$  is the amount of configuration memory [61].

## RESULTS

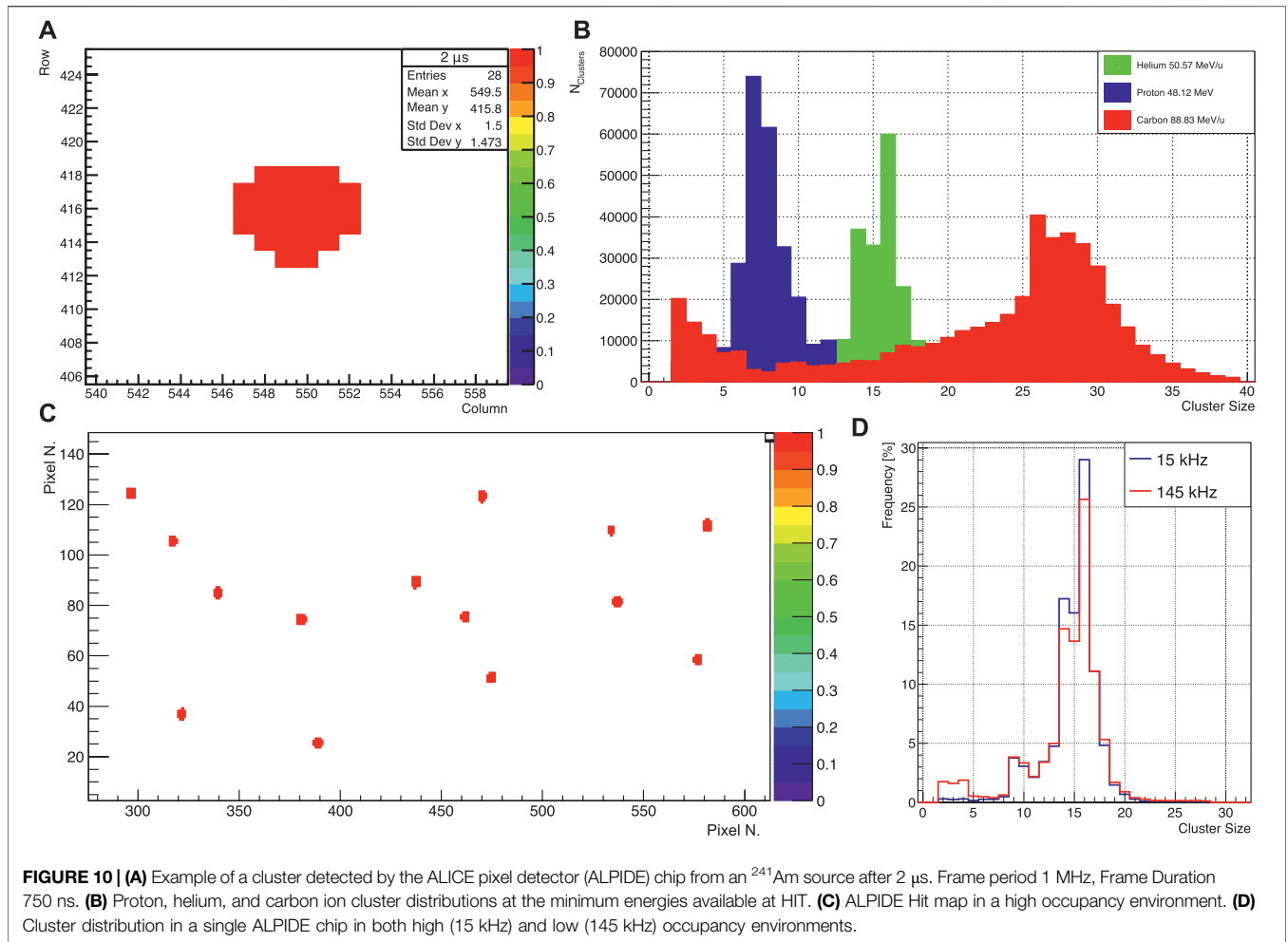
### ALPIDE Response

The ALPIDE chips were intensively tested to verify their response to different radiation field as described above. Exposing the ALPIDE chip to an  $^{241}\text{Am}$  source, the evolution of the cluster shape could be observed using a 1 MHz data frame period with a frame duration of 750 ns. The signal produced by the  $^{241}\text{Am}$  source has a time over threshold 4–6  $\mu\text{s}$ , so for each pulse (every 1  $\mu\text{s}$ ), a data frame window matched up with the signal from the analog frontend and the hit was read out. This allowed to have the same cluster in several consequent frames. In **Figure 10A** an example of a typical cluster registered on a readout frame is reported.

In **Figure 10B** the cluster size distributions for proton, helium, and carbon ion beams at the minimum available energies at HIT (48.12 MeV, 50.57 MeV/u, and 88.83 MeV/u, respectively) are shown. As expected, the cluster size is bigger for higher linear energy transfer (LET) radiation (i.e., carbon). A second peak for small size cluster is visible for ions (more prominent for carbon) which can be attributed to nuclear fragments produced along the beam line or on the metal layer on top of the ALPIDE chip. In **Figure 10C** a hit-map on the single ALPIDE chip in a high occupancy environment for a 50.57 MeV/u helium beam is reported.

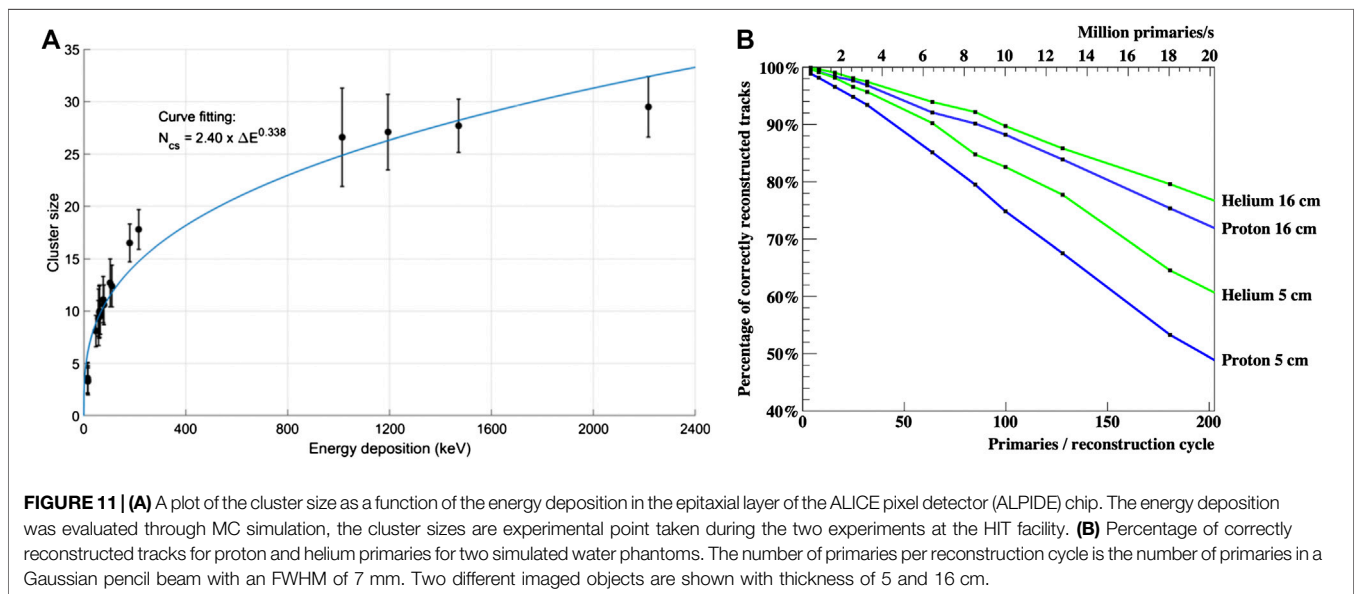
For the low (15 kHz particle rate) and high (145 kHz) occupancy runs, an average of 55.91 and 934.6 pixels firing per frame (corresponding to 0.01 and 0.17% of the total number of pixels in the ALPIDE) was readout by the ALPIDE, respectively. As shown in **Figure 10D**, the distributions are similar in shape for both high and low occupancy environments, confirming that the ALPIDE response is independent of occupancy.

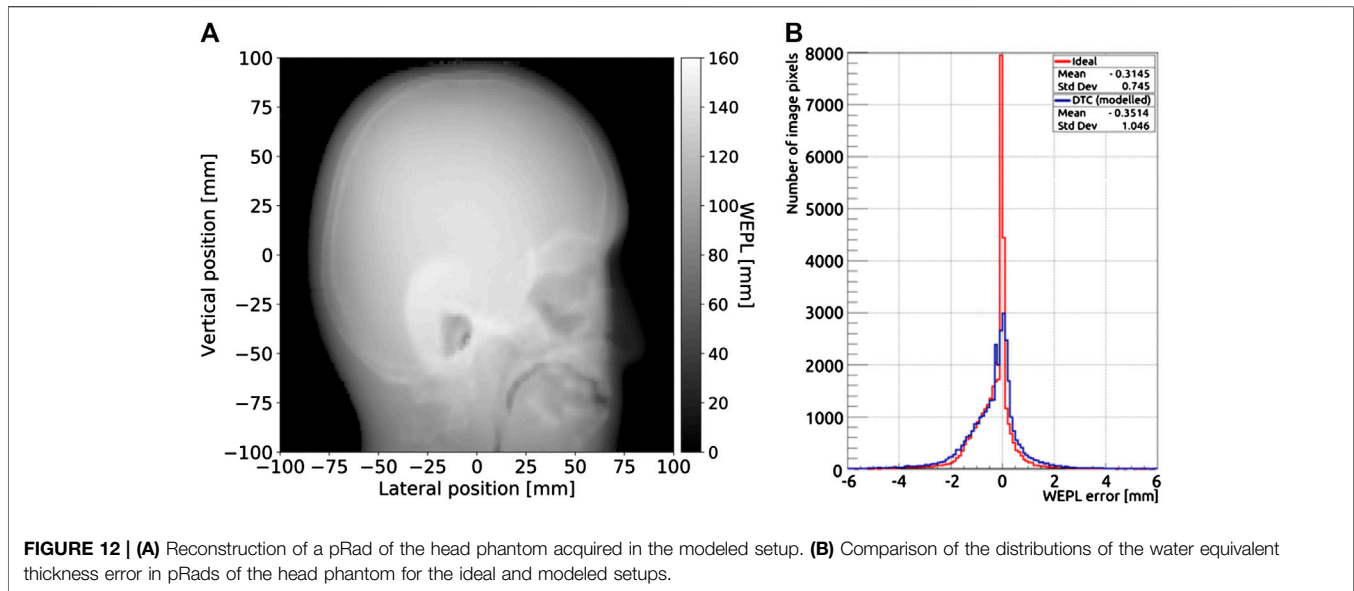
In **Figure 11A** a plot of the cluster size as a function of the energy deposited on the epitaxial layer of the ALPIDE is shown. The energy deposited for different energies and particles was evaluated through the MC simulation of the 25  $\mu\text{m}$  thick silicon epitaxial layer of the ALPIDE chip. The experimental data were taken from both the experiments at HIT. The points reported in the plot represent the mean of the Gaussian fit of the cluster distributions and the error bars are given by the standard deviations of such Gaussians. The relation shown in **Figure 11A**, together with a Bragg-Kleeman depth dose curve will be used to reconstruct tracks inside the DTC, allowing for precise range fitting, for rejection of nuclear events and for particle identification in the case of ion imaging, as explained above. In **Figure 11B** the fraction of correctly reconstructed



tracks using proton and helium primaries crossing two simulated cubic water phantoms with 5 and 16 cm size is shown. The study was performed on charge diffused MC data. For helium ions, less

affected by scattering while crossing the object under study, a higher number of tracks correctly reconstructed was obtained for both phantoms [64]. The track reconstruction process currently





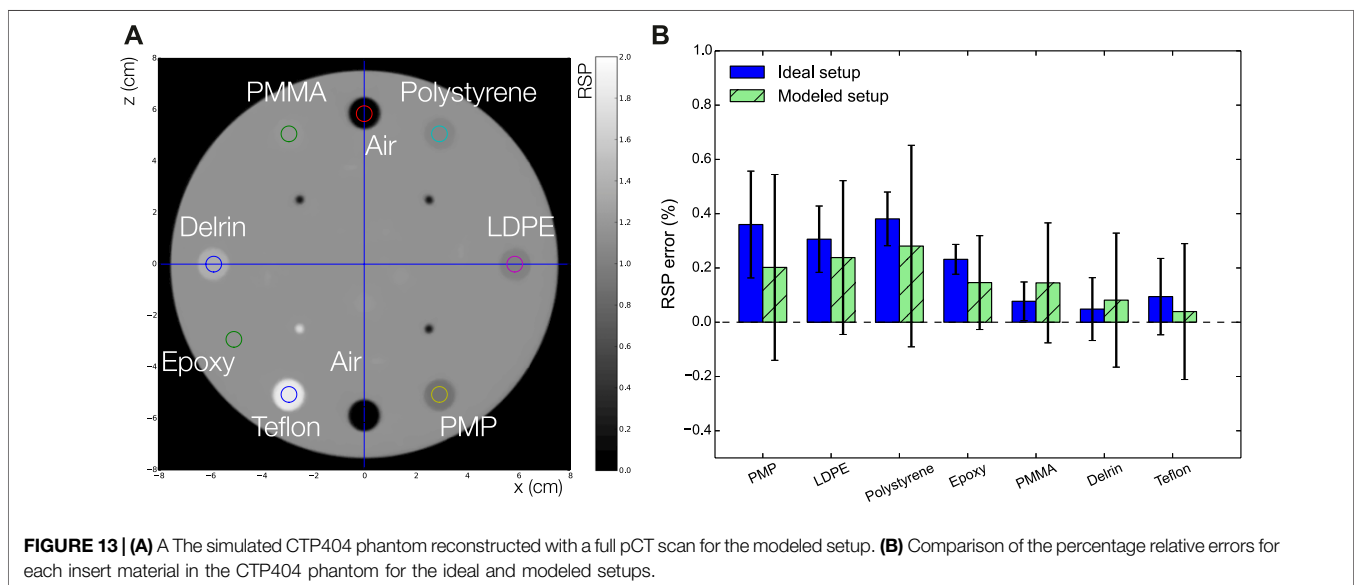
requires approximately 1.5 ms per primary track using a single Intel® Xeon® GOLD 6136 CPU @ 3 GHz. Thus, a pRad containing four million primaries could be acquired at ~0.5 s, with a reconstruction time of 2 min on the 48 available cores. However, the track reconstruction algorithm is suitable for GPU vectorization and this would further reduce the execution time.

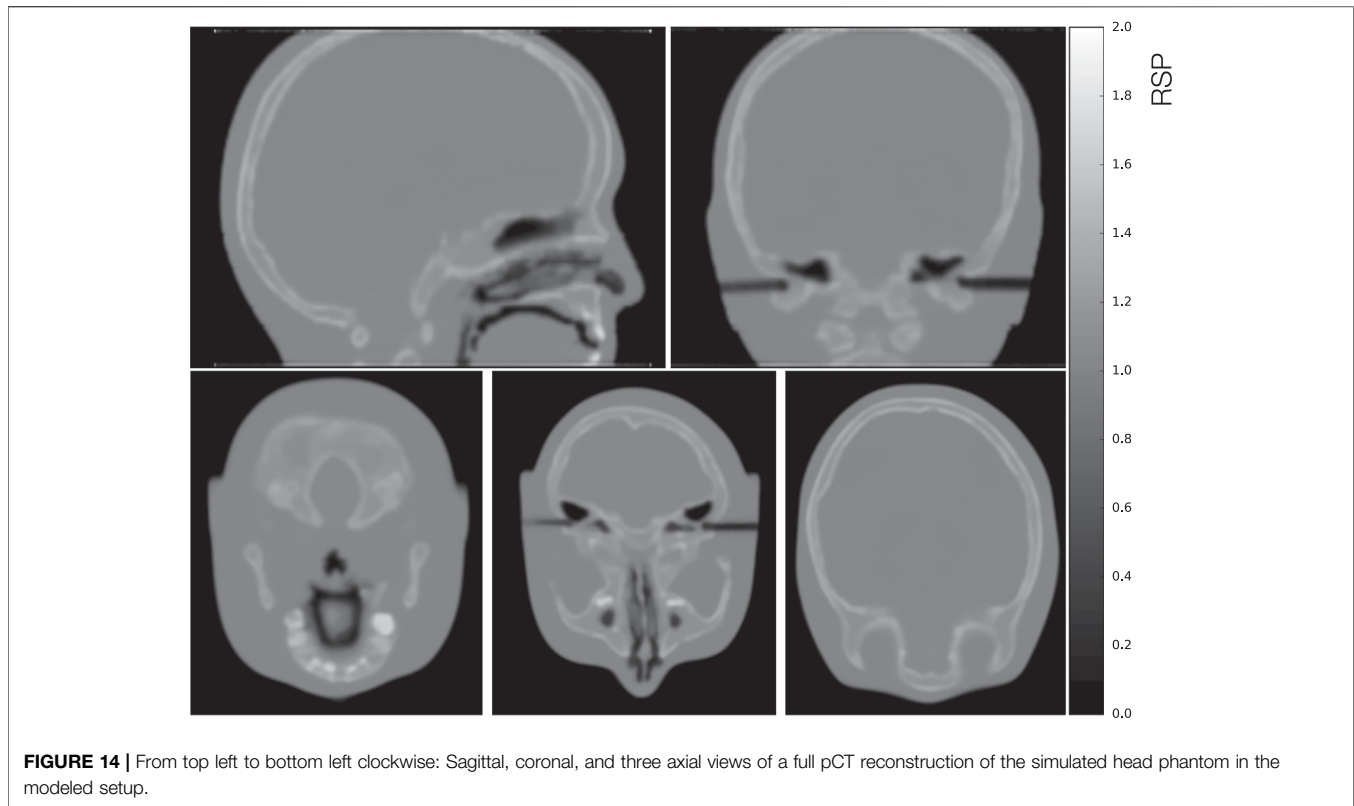
### Reconstructed Images from Simulation

In **Figure 12A** a pRad of the head phantom in the modeled DTC setup is shown. In **Figure 12B** a comparison of the distributions of the WEPL errors in pRad reconstruction for the ideal and the modeled setup is shown. The error distribution results wider for the modeled setup than for the ideal setup, 0.745 mm standard deviation of the ideal compared to the modeled 1.045 mm. For the modeled setup,

a higher error is observed in the facial structures consisting of high gradient regions.

The CTP404 phantom reconstructed with a simulated full pCT scan is shown in **Figure 13A** using the DTC modeled setup. In **Figure 13B** a comparison of the average RSP percent errors (calculated as the difference between the reconstructed value and the reference value, divided by the reference value) for each material in the CTP404 phantom (excluding air) for the ideal and the modeled setups is shown. The mean RSP values were measured in a small area (shown in **Figure 13A** by the small colored circles) in the center of each insert and averaged over 10 reconstructed slices. The error bars represent the relative standard deviation of each RSP distribution. For both the setups the RSP error for each material is below 0.5%. Although in most cases (except for PMMA and Delrin) the





RSP error is smaller for the modeled setup than the ideal, the error bars for the modeled setup are sometimes two times as big as the errors, indicating a high level of noise for the modeled setup. The average error for all the materials in the CTP404 phantom is 0.214 and 0.162% for the ideal and the modeled setups, respectively. In **Figure 14** different views of the head phantom reconstructed for the modeled setup are shown. The images result clean with no artifacts and all the salient structures in the head (brain, bones, teeth, and air cavities) are well distinguishable. The reconstruction time for these images was 4,383.17 s (about 1.5 h) using an Intel® Xeon® E5-2697 v2 CPU @ 2.70GHz with 48 cores, and an NVIDIA® GeForce GTX 650 GPU.

## Radiation Damage

Based on the observed fluence and dose deposited inside FPGA objects and inside the DTC, the expected SEU rate and time until FPGA and ALPIDE reach their respective TID and NIEL limits are collected in **Table 1**. According to **Eq. 1**, a single SEU event for the full system every 2,933 s is expected at a distance of 200 cm, considering  $\sigma_{SEU}$  equal to  $1.89 \times 10^{-15} \text{ cm}^2/\text{bit}$  for the employed FPGAs [65] with a configuration memory of 512 Mbit.

## DISCUSSION

The work presented is a report of the design and development of the Bergen pCT scanner. The most distinguishable characteristic of the detector is the high granularity DTC which functions both

**TABLE 1** | Expected FPGA and ALPIDE health and lifetime from being exposed in both pCT and proton therapy.

Distance from DTC (cm)	pCT	Proton therapy	
	Time (s)	Time (s)	
1 SEU			
10	20.4	8.0	
50	197.2	66.2	
100	689.7	224.7	
200	2,932.6	1,022.5	
300	6,410.3	2,415.5	
400	11,286.7	4,329.0	
Dose (TID-limit)	Lifetime (s)	Lifetime (s)	
10	$1.40 \times 10^{10}$	$1.14 \times 10^{10}$	
50	$1.23 \times 10^{11}$	$7.66 \times 10^{10}$	
100	$6.02 \times 10^{11}$	$2.89 \times 10^{11}$	
200	$4.12 \times 10^{12}$	$1.14 \times 10^{12}$	
300	$6.45 \times 10^{12}$	$2.35 \times 10^{12}$	
400	$1.43 \times 10^{13}$	$3.91 \times 10^{12}$	
Peak values in the ALPIDE	Dose (TID) NIEL limit	$2.89 \times 10^8 \text{ s}$ $1.94 \times 10^8 \text{ s}$	$2.88 \times 10^8 \text{ s}$ $1.69 \times 10^8 \text{ s}$

ALPIDE, ALICE pixel detector; DTC, digital tracking calorimeter; pCT, proton CT. All the 43 FPGAs are considered as a single system and the time it takes for a single SEU to occur is estimated (1 SEU). A conservative TID limit of 100 Gy for the FPGA is used. The ALPIDE design limits are 27,000 Gy and  $1.7 \times 10^{13} \text{ MeV n}_{eq} \text{ cm}^{-2}$  for TID and NIEL limits, respectively, as given in Mager et al. [38]. A safety factor of 10 is included in all calculations and estimations.

as tracking system and energy/range detector, allowing a high multiplicity of incoming particle tracks to be reconstructed simultaneously. Starting from the basic ALPIDE chip, the final

prototype scanner will have a size (27 cm × 16.6 cm) big enough to image at least a human head in a single DAQ run. To achieve the necessary area, the ALPIDE chips will be bounded side by side in strings of nine mounted in flex cable which will be in turn glued on an aluminum carrier. The system comprises 43 degrader/sensor sandwiches (2 used for the rear trackers, 41 for the calorimeter) forming a single assembly, the DTC. Thanks to the technology employed, the tracker system and the calorimeter will employ the same basic sensor, the ALPIDE chip, allowing a simplification of the readout.

As described in *The Digital Tracking Calorimeter Electronics*, the electronic system is based on a trigger-less readout architecture and designed to continuously capture data with minimal integration time over a short period of time. With these features, a capture rate of 10 μs with a gap of roughly 250 ns for only few seconds will provide enough data for a single 2D-image. Therefore, a readout sequence will be started from the control room, and a single readout unit will act as a master and initiate the continuous pulse sequence from the other readout units. The dimension of a head radiograph is approximately 18 cm × 18 cm, and about 100 primaries/mm<sup>2</sup> after filtering are necessary for the reconstruction. Considering object and detector attenuation, track reconstruction and the whole image generation process, an effective survival rate of at least 40% can be expected for protons. This would mean that ~6 M primaries for an image are needed and since 100 primaries per readout cycle can be comfortably reconstructed, with a frame time of 10 μs this corresponds to 10 M primary particles/s, that is about half a second per radiograph. For a full pCT scan, assuming 100 primaries/mm<sup>3</sup> (according to Johnson et al. [66]) for a head volume of 2.26 × 10<sup>6</sup> mm<sup>3</sup>, 560 M histories would be needed. This corresponds to ~60 s for a full CT acquisition and it means that the system is fast enough to be used in a clinical environment, capable to handle the high-rate medical beams used in treatment centers. The final system will be able to handle a beam frequency comparable to or better than the pCT systems currently available can manage [15], depending on the scanning modality and the beam spot size.

To allow future system upgrades, the electronics, integrated with the mechanical design, was designed with scalability in mind. Each layer of the detector requires identical units of electronics. Adding more layers to the detector will only require duplication of existing hardware and firmware. For this reason, all communication to the control room is done via Ethernet protocols, allowing simple connections of switches to add more layers. The optimized choice of chip cables and string FPCs for the system will allow a good handling of jitter and noise on the high-speed links. Regarding the readout software, a few host machines will be enough to run the applications needed to unpack and sort ALPIDE chip data and serve the full data readout. The applications can be controlled by a SCADA, a decision about the concrete Run Control system will be taken based on the experience with the prototype system. Upcoming DAQ systems, like ALICE O2, are being developed with distributed workflows in mind and can process the extreme high bandwidths requirements of upcoming LHC experiments.

The same system could be also beneficial to improve the speed of data handling during a pCT scan.

Based on the TID and NIEL radiation hardness of the ALPIDE (**Table 1**) the DTC will not reach its TID limit until after 289 Ms (9.2 years) and NIEL limit after 194 Ms (6.2 years) of constant exposure to radiation from pCT. The full system with all the FPGA components at a lateral distance of 200 cm from the DTC is expected to experience a single SEU only every 2,933 s. The DTC is therefore expected to be sufficiently radiation tolerant to survive and stay healthy in the radiation environment inside a treatment room for several years without losing operational efficiency.

The preliminary experiments conducted on the single ALPIDE chip have shown the capability of the ALPIDE to handle high rate beam spills. As shown in **Figure 10D**, the chip will respond equally in both a high or low occupancy environments, giving the same averaged cluster size for particles with the same initial energy. The ALPIDE sensor response was therefore proved to be independent of occupancy. The ALPIDE was also successfully tested for higher LET beams (helium and carbon ions) showing a clear difference in response for different charged particles, even when the initial energy per nucleon was similar (**Figure 10B**). The bias voltage was set to 0 V for the experiments reported in this work. However, the use of non-zero bias could reduce the size of the clusters, enhancing the resolution of the hit position measurements. For this reason, the ALPIDE chips composing the tracker layers will be operated in bias mode. With the data collected at the HIT facility for different ion species at various energies spread all over the energy range available, it was possible to extrapolate a curve of the dependency of the cluster size on the energy deposited on the ALPIDE epitaxial layer. Thanks to the tracking algorithm and the different cluster size distributions generated from each different ion species the DTC will function as a continuous tracking device able to collect a topology of different interactions, such as hadronic processes or Coulomb scattering, which will present very different trajectory path and cluster distributions all over the 43 layers of the DTC. This will allow, prior to the reconstruction process, to discriminate different particles at different energies, meaning that it will be possible to distinguish a primary (useful for the reconstruction) from a secondary (to be discarded). First investigations about distinguishing secondary particles from primary helium ions in the DTC can be found in Pettersen et al. [64].

For the modeled MC simulation, pRad, and pCT reconstructions showed encouraging results for WEPL and RSP accuracy. The modeled setup gave results comparable to the ideal setup for both pRad and pCT, reflecting the expected performances of the DTC. The mean RSP error for the reconstructed material in the CTP404 phantom was better than 0.2% for the modeled setup.

However, the mean accuracy was better than that for the ideal system. The reason could depend on the sampling from a Gaussian distribution of the WEPL blurring, which provides more flexibility to the optimization in the modeled setup rather than the ideal one. Nevertheless, the mean RSP accuracy per insert for modeled and

ideal setup agree with each other within their uncertainty. In addition, there is a large variance in the per-voxel RSP accuracy (represented by the large error bars in **Figure 13B**) present for the modeled case, as expected from the increased WEPL noise.

The pCT of the head phantom yielded clear artifact-free images, enabling the distinction of different anatomical features. However, it has to be noted that the modeled setup here presents somewhat of an ideal case scenario for the DTC performance: the accuracy of the track reconstruction in the DTC is subject to the impinging particle fluence. An increased particle fluence leads to an increased confusion of tracks, which for heterogeneous objects may influence the systematic and stochastic WEPL uncertainty. Future efforts will optimize the number of correctly reconstructed tracks in the DTC, potentially utilizing machine learning methods. Nevertheless, the overall performance of the DTC can be expected to fulfill the goal of achieving an RSP accuracy of better than 1%. The spatial resolution achievable with a single sided pCT setup was not object of the present work, but it was investigated in a previous publication [37]. A reduced performance was observed compared to that of an imaging system comprising also front tracking detectors, as expected. However, the obtained spatial resolution might be sufficient for treatment planning, where usually relatively large voxel sizes are used (typically 1 mm × 1 mm × 2 mm) so that the low sampling frequency provided by these voxels relaxes the requirement on spatial resolution. Krah et al. [56] have calculated a value of 0.3 line-pair/mm as lower limit spatial resolution needed for treatment planning. The demand on spatial resolution is therefore not very strict. A full comparison in terms of spatial resolution, noise and RSP accuracy of the DTC pCT image reconstructions to the performance of other existing pCT prototype systems will be the subject of further investigations.

At the time of writing, the device is under construction, the ALPIDE mass production has started and the first ALPIDE strings are being bonded and will be ready to be tested soon. After the testing the assembly phase will follow and the first full setup will be ready to be installed in medical facilities, presumably in 2 years. Once ready, thanks to its ability to detect and distinguish different types of radiation and its specific design, the pCT scanner can be employed not solely for proton imaging but also for additional online applications during the treatment allowing motion tracking during respiration, complementing other X-ray or surfaced based methods [67]. Given the lack of the front tracker, the detector could be positioned downstream of the patient during the treatment with a carbon-helium mixed beam, where carbon ions would be used for treatment and helium ions would be used for verification [67]. Furthermore, placing the detector beside the treated patient at an opportune angle, secondary radiation (e.g., charged nuclear fragments, neutron) originating from the Bragg peak area could be tracked for *in situ* range verification.

## REFERENCES

1. Wilson RR. Radiological use of fast protons. *Radiology* (1946) 47(5):487–91. doi:10.1148/47.5.487
2. Lomax AJ. Myths and realities of range uncertainty. *Br J Radiol* (2020) 93(1107): 20190582. doi:10.1259/bjr.20190582

## DATA AVAILABILITY STATEMENT

The raw data supporting the conclusions of this article will be made available by the authors, without undue reservation.

## AUTHOR CONTRIBUTIONS

DR supervised the full project, PP structured and organized the whole manuscript. SM, AB, FW, GB, and ÅS worked on the mechanical design of the DTC and contribute to the writing of relative sections. OG, MR, TB, AH, ØJ, VE, KU, and HH developed the electronics and readout software and contributed to the writing of the concerning sections. VB, IT, MP, and OL were responsible for the developing, designing and creating of the chip cables, the multi-layered flexes, and the string prototypes. HP developed the tracking algorithm and wrote the related section and. HP and JRS built and run the MC simulations used for the imaging reconstruction. JRS studied the effect of radiation on the electronics and wrote the relative section. LV, JS, and SB made possible and arranged the experiments at the HIT facility. LV, OG, VE, QM, MK, ÅS, GT, JRS, and PP collaborated directly to the experiments at HIT and at the elaboration of the collected data. VE and ATS created the plots shown in the experimental results. PP and LV produced the reconstructed pCT images. The remaining co-authors contributed to the conception and the developing of the project participated in the review process of the manuscript.

## FUNDING

This work is supported by the Research Council of Norway (Norges forskningsråd), grant number 250858; the Trond Mohn Foundation, grant number BFS2017TMT07; and the Hungarian National Research, Development and Innovation Office (NRDIO) OTKA K120660 and 2019-2.1.6-859NEMZ\_KI-2019-00011 grants.

## ACKNOWLEDGMENTS

The authors would like to thank the HIT facility for providing beam time, and the HIT accelerator engineers for helping with the beam delivery and the Thailand Center of Excellence in Physics and Development and Promotion of Science and Technology Talents Project (DPST) for supporting the Suranaree University of Technology (Nakhon Ratchasima, Thailand) on the pCT project.

3. Schneider U, Pedroni E, Lomax A. The calibration of CT Hounsfield units for radiotherapy treatment planning. *Phys Med Biol* (1996) 41(1):111–24. doi:10.1088/0031-9155/41/1/009
4. Paganetti H. Range uncertainties in proton therapy and the role of Monte Carlo simulations. *Phys Med Biol* (2012) 57(11):R99–117. doi:10.1088/0031-9155/57/11/r99
5. Yang M, Zhu XR, Park PC, Titt U, Mohan R, Virshup G, et al. Comprehensive analysis of proton range uncertainties related to patient stopping-power-ratio

- estimation using the stoichiometric calibration. *Phys Med Biol* (2012) **57**(13):4095–115. doi:10.1088/0031-9155/57/13/4095
6. Cormack AM. Representation of a function by its line integrals, with some radiological applications. *J Appl Phys* (1963) **34**(9):2722–7. doi:10.1063/1.1729798
  7. Collins-Fekete CA, Volz L, Portillo SK, Beaulieu L, Seco J. A theoretical framework to predict the most likely ion path in particle imaging. *Phys Med Biol* (2017) **62**(5):1777–90. doi:10.1088/1361-6560/aa58ce
  8. Schulte RW, Penfold SN, Tafas JT, Schubert KE. A maximum likelihood proton path formalism for application in proton computed tomography. *Med Phys* (2008) **35**(11):4849–56. doi:10.1118/1.2986139
  9. Williams DC. The most likely path of an energetic charged particle through a uniform medium. *Phys Med Biol* (2004) **49**(13):2899–911. doi:10.1088/0031-9155/49/13/010
  10. Hansen DC, Seco J, Sørensen TS, Petersen JBB, Wildberger JE, Verhaegen F, et al. A simulation study on proton computed tomography (CT) stopping power accuracy using dual energy CT scans as benchmark. *Acta Oncol* (2015) **54**(9):1638–42. doi:10.3109/0284186x.2015.1061212
  11. Penfold SN, Rosenfeld AB, Schulte RW, Schubert KE. A more accurate reconstruction system matrix for quantitative proton computed tomography. *Med Phys* (2009) **36**(10):4511–8. doi:10.1118/1.3218759
  12. Penfold SN, Schulte RW, Censor Y, Rosenfeld AB. Total variation superiorization schemes in proton computed tomography image reconstruction. *Med Phys* (2010) **37**(11):5887–95. doi:10.1118/1.3504603
  13. Poludniowski G, Allinson NM, Evans PM. Proton computed tomography reconstruction using a backprojection-then-filtering approach. *Phys Med Biol* (2014) **59**(24):7905–18. doi:10.1088/0031-9155/59/24/7905
  14. Rit S, Dedes G, Freud N, Sarrut D, Létang JM. Filtered backprojection proton CT reconstruction along most likely paths. *Med Phys* (2013) **40**(3):031103. doi:10.1118/1.4789589
  15. Johnson RP. Review of medical radiography and tomography with proton beams. *Rep Prog Phys* (2018) **81**(1):016701. doi:10.1088/1361-6633/aa8b1d
  16. Poludniowski G, Allinson NM, Evans PM. Proton radiography and tomography with application to proton therapy. *Br J Radiol* (2015) **88**(1053):20150134. doi:10.1259/bjr.20150134
  17. Esposito M, Waltham C, Taylor JT, Manger S, Phoenix B, Price T, et al. PRaVDA: the first solid-state system for proton computed tomography. *Phys Med* (2018) **55**:149–54. doi:10.1016/j.ejmp.2018.10.020
  18. Giacometti V, Bashkirov VA, Piersimoni P, Guatelli S, Plautz TE, Sadrozinski HF, et al. Software platform for simulation of a prototype proton CT scanner. *Med Phys* (2017) **44**(3):1002–16. doi:10.1002/mp.12107
  19. Piersimoni P, Ramos-Mendez J, Geoghegan T, Bashkirov VA, Schulte RW, Faddegon BA. The effect of beam purity and scanner complexity on proton CT accuracy. *Med Phys* (2017) **44**(1):284–98. doi:10.1002/mp.12013
  20. Plautz TE, Bashkirov V, Giacometti V, Hurley RF, Johnson RP, Piersimoni P, et al. An evaluation of spatial resolution of a prototype proton CT scanner. *Med Phys* (2016) **43**(12):6291–300. doi:10.1118/1.4966028
  21. Dedes G, Dickmann J, Niepel K, Wesp P, Johnson RP, Pankuch M, et al. Experimental comparison of proton CT and dual energy x-ray CT for relative stopping power estimation in proton therapy. *Phys Med Biol* (2019) **64**(16):165002. doi:10.1088/1361-6560/ab2b72
  22. Yang M, Virshup G, Clayton J, Zhu XR, Mohan R, Dong L. Theoretical variance analysis of single- and dual-energy computed tomography methods for calculating proton stopping power ratios of biological tissues. *Phys Med Biol* (2010) **55**(5):1343–62. doi:10.1088/0031-9155/55/5/006
  23. Depauw N, Seco J. Sensitivity study of proton radiography and comparison with kV and MV x-ray imaging using GEANT4 Monte Carlo simulations. *Phys Med Biol* (2011) **56**(8):2407–21. doi:10.1088/0031-9155/56/8/006
  24. Schulte RW, Bashkirov V, Loss Klock MC, Li T, Wroe AJ, Evseev I, et al. Density resolution of proton computed tomography. *Med Phys* (2005) **32**(4):1035–46. doi:10.1118/1.1884906
  25. Collins-Fekete C-A, Volz L, Portillo SKN, Beaulieu L, Seco J. A theoretical framework to predict the most likely ion path in particle imaging. *Phys Med Biol* (2017) **62**(5):1777–90. doi:10.1088/1361-6560/aa58ce
  26. Gehrke T, Gallas R, Jäkel O, Martišiková M. Proof of principle of helium-beam radiography using silicon pixel detectors for energy deposition measurement, identification, and tracking of single ions. *Med Phys* (2018) **45**(2):817–29. doi:10.1002/mp.12723
  27. Hansen DC, Bassler N, Sørensen TS, Seco J. The image quality of ion computed tomography at clinical imaging dose levels. *Med Phys* (2014) **41**(11):111908. doi:10.1118/1.4897614
  28. Magallanes L, Meyer S, Gianoli C, Kopp B, Voss B, Jäkel O, et al. Upgrading an integrating carbon-ion transmission imaging system with active scanning beam delivery toward low dose ion imaging. *IEEE Trans Radiat Plasma Med Sci* (2020) **4**(2):262–8. doi:10.1109/trpms.2019.2948584
  29. Martišiková M, Gehrke T, Berke S, Aricò G, Jäkel O. Helium ion beam imaging for image guided ion radiotherapy. *Radiat Oncol* (2018) **13**(1):109. doi:10.1186/s13014-018-1046-6
  30. Piersimoni P, Faddegon BA, Mendez JR, Schulte RW, Volz L, Seco J. Helium CT: Monte Carlo simulation results for an ideal source and detector with comparison to proton CT. *Med Phys* (2018) **45**(7):3264–74. doi:10.1002/mp.12942
  31. Volz L, Piersimoni P, Bashkirov VA, Brons S, Collins-Fekete C-A, Johnson RP, et al. The impact of secondary fragments on the image quality of helium ion imaging. *Phys Med Biol* (2018) **63**(19):195016. doi:10.1088/1361-6560/aadf25
  32. De Haas AP, Nooren G, Peitzmann T, Reicher M, Rocco E, Röhrich D, et al. The FoCal prototype—an extremely fine-grained electromagnetic calorimeter using CMOS pixel sensors. *J Inst Met* (2018) **13**(01):P01014. doi:10.1088/1748-0221/13/01/p01014
  33. Rocco E. Highly granular digital electromagnetic calorimeter with MAPS. *Nucl Part Phys Proc* (2016) **273–275**:1090–5. doi:10.1016/j.nuclphysbps.2015.09.171
  34. Pettersen HES. *A digital tracking calorimeter for proton computed tomography*. [PhD thesis]. Bergen (Norway): University of Bergen (2018)
  35. Pettersen HES, Alme J, Biegun A, Van Den Brink A, Chaar M, Fehlker D, et al. Proton tracking in a high-granularity digital tracking calorimeter for proton CT purposes. *Nucl Instrum Methods Phys Res A* (2017) **860**:51–61. doi:10.1016/j.nima.2017.02.007
  36. Pettersen HES, Alme J, Barnaföldi GG, Barthel R, Van Den Brink A, Chaar M, et al. Design optimization of a pixel-based range telescope for proton computed tomography. *Phys Med* (2019) **63**:87–97. doi:10.1016/j.ejmp.2019.05.026
  37. Sölje JR, Volz L, Pettersen HES, Piersimoni P, Odland OH, Roehrich D, et al. Image quality of list-mode proton imaging without front trackers. *Phys Med Biol* (2020) **65**(13):135012. doi:10.1088/1361-6560/ab8ddb
  38. Mager M. ALPIDE, the monolithic active pixel sensor for the ALICE ITS upgrade. *Nucl Instrum Methods Phys Res B* (2016) **824**:434–8. doi:10.1016/j.nima.2015.09.057
  39. Yang P, Aglieri G, Cavicchioli C, Chalmet PL, Chanlek N, Collu A, et al. Low-power priority address-encoder and reset-decoder data-driven readout for monolithic active pixel sensors for tracker system. *Nucl Instrum Methods Phys Res B* (2015) **785**:61–9. doi:10.1016/j.nima.2015.02.063
  40. Aglieri Rinella G. The ALPIDE pixel sensor chip for the upgrade of the ALICE inner tracking system. *Nucl Instrum Methods Phys Res B* (2017) **845**:583–7. doi:10.1016/j.nima.2016.05.016
  41. Poonsawat W, Kobdaj C, Sitta M, Yan Y. Stave module design and development of the new ALICE inner tracking system. *J Instrum* (2019) **14**(05):P05003. doi:10.1088/1748-0221/14/05/p05003
  42. Zherebchevsky VI, Altsybeev IG, Feofilov GA, Francescon A, Gargiulo C, Igolkin SN, et al. Experimental investigation of new ultra-lightweight support and cooling structures for the new inner tracking system of the ALICE detector. *J Instrum* (2018) **13**(08):T08003. doi:10.1088/1748-0221/13/08/t08003
  43. Bopp C, Rescigno R, Rousseau M, Brasse D. The impact of tracking system properties on the most likely path estimation in proton CT. *Phys Med Biol* (2014) **59**(23):N197–210. doi:10.1088/0031-9155/59/23/n197
  44. Šuljić M. ALPIDE: the monolithic active pixel sensor for the ALICE ITS upgrade. *J Instrum* (2016) **11**:C11025. doi:10.1088/1748-0221/11/11/c11025
  45. Sudár Á. *Measurement of the temperature distribution inside a calorimeter*. [BSc thesis]. Budapest (Hungary): Budapest University of Technology and Economics (2020)
  46. IEEE standard systemC(R) language reference manual. In: IEEE Std 1666-2005; 2006 Mar 31; IEEE. p. 1–423. doi:10.1109/IEEESTD.2006.99475

47. Grøttvik O, Alme J, Barthel R, Bodova T, Borshchov V, Van den Brink A, et al. Development of readout electronics for a digital tracking calorimeter. In: Topical workshop on electronics for particle physics; 2020 Mar (2019) p. 370. doi:10.22323/1.370.0090
48. Borshchov VM, Listratenko OM, Protsenko MA, Tymchuk IT, Fomin OO. Innovative microelectronic technologies for high-energy physics experiments. *Met Funct Mater* (2017) **23**(4):143–53. doi:10.15407/fm24.01.143
49. Larrea CG, Harder K, Newbold D, Sankey D, Rose A, Thea A, et al. IPbus: a flexible Ethernet-based control system for xTCA hardware. *J Instrum* (2015) **10**(02):C02019. doi:10.1088/1748-0221/10/02/c02019
50. Strandlie A, Frühwirth R. Track and vertex reconstruction: from classical to adaptive methods. *Rev Mod Phys* (2010) **82**(2):1419–58. doi:10.1103/revmodphys.82.1419
51. Pettersen HES, Meric I, Odland OH, Shafiee H, Sölje JR, Röhrich D. Proton tracking algorithm in a pixel-based range telescope for proton computed tomography. In: CTD2018 EPJ web of conferences; 2018 Mar 20–22; Seattle, WA (Forthcoming 2018) Available from: <https://arxiv.org/abs/2006.09751> (Accessed June 2020).
52. Jan S, Benoit D, Becheva E, Carlier T, Cassol F, Descourt P, et al. GATE V6: a major enhancement of the GATE simulation platform enabling modelling of CT and radiotherapy. *Phys Med Biol* (2011) **56**(4):881–901. doi:10.1088/0031-9155/56/4/001
53. Jan S, Santin G, Strul D, Staelens S, Assié K, Autret D, et al. GATE: a simulation toolkit for PET and SPECT. *Phys Med Biol* (2004) **49**(19):4543–61. doi:10.1088/0031-9155/49/19/007
54. Agostinelli S, Allison J, Amako K, Apostolakis J, Araujo H, Arce P, et al. Geant4—a simulation toolkit. *Nucl Instrum Methods Phys Res A* (2003) **506**(3):250–303. doi:10.1016/s0168-9002(03)01368-8
55. Allison J, Amako K, Apostolakis J, Araujo H, Arce Dubois P, Asai M, et al. Geant4 developments and applications. *IEEE Trans Nucl Sci* (2006) **53**(1):270–8. doi:10.1109/tns.2006.869826
56. Krah N, Khellaf F, Letang JM, Rit S, Rinaldi I. A comprehensive theoretical comparison of proton imaging set-ups in terms of spatial resolution. *Phys Med Biol* (2018) **63**(13):135013. doi:10.1088/1361-6560/aacalf
57. Grevillot L, Bertrand D, Dessy F, Freud N, Sarrut D. GATE as a GEANT4-based Monte Carlo platform for the evaluation of proton pencil beam scanning treatment plans. *Phys Med Biol* (2012) **57**(13):4223–44. doi:10.1088/0031-9155/57/13/4223
58. Volz L, Piersimoni P, Johnson RP, Bashkirov VA, Schulte RW, Seco J. Improving single-event proton CT by removing nuclear interaction events within the energy/range detector. *Phys Med Biol* (2019) **64**(15):15NT01. doi:10.1088/1361-6560/ab2671
59. Collins-Fekete CA, Brousmiche S, Portillo SK, Beaulieu L, Seco J. A maximum likelihood method for high resolution proton radiography/proton CT. *Phys Med Biol* (2016) **61**(23):8232–48. doi:10.1088/0031-9155/61/23/8232
60. Collins-Fekete C-A, Doolan P, Dias MF, Beaulieu L, Seco J. Developing a phenomenological model of the proton trajectory within a heterogeneous medium required for proton imaging. *Phys Med Biol* (2015) **60**(13):5071–82. doi:10.1088/0031-9155/60/13/5071
61. Røed K. *Single event upsets in SRAM FPGA based readout electronics for the time projection chamber in the ALICE experiment*. [Doctoral thesis]. Bergen (Norway): University of Bergen (2009)
62. Böhlen TT, Cerutti F, Chin MPW, Fassò A, Ferrari A, Ortega PG, et al. The FLUKA code: developments and challenges for high energy and medical applications. *Nucl Data Sheets* (2014) **120**:211–4. doi:10.1016/j.nds.2014.07.049
63. Ferrari A, Sala PR, Fassò A, Ranft J. *FLUKA: a multi-particle transport code*. Report No.: INFN-TC-05-11. Geneva, Switzerland: CERN (2005)
64. Pettersen HES, Volz L, Sölje JR, Alme J, Barnaföldi GG, Barthel R, et al. *Helium radiography with a digital tracking calorimeter—a Monte Carlo study for secondary track rejection*. Manuscript submitted to Physics in Medicine and Biology (2020)
65. Hiemstra DM, Kirischian V, Brelski J. Single event upset characterization of the Kintex UltraScale field programmable gate array using proton irradiation. In: IEEE radiation effects data workshop (REDW); 2016 June 11–15; Portland, United States (2016) p. 1–5.
66. Johnson RP, Bashkirov V, Dewitt L, Giacometti V, Hurley RF, Piersimoni P, et al. A fast experimental scanner for proton CT: technical performance and first experience with phantom scans. *IEEE Trans Nucl Sci* (2016) **63**(1):52–60. doi:10.1109/tns.2015.2491918
67. Spadea MF, Baroni G, Gierra DP, Turcotte JC, Chen GTY, Sharp GC. Evaluation and commissioning of a surface based system for respiratory sensing in 4D CT. *J Appl Clin Med Phys* (2011) **12**(1):162–169.
68. Kim D, Rinella GA, Cavicchioli C, Chanlek N, Collu A, Degerli Y, et al. Front end optimization for the monolithic active pixel sensor of the ALICE inner tracking system upgrade. *J Inst Met* (2016) **11**(02):C02042. doi:10.1088/1748-0221/11/02/c02042

**Conflict of Interest:** The authors declare that the research was conducted in the absence of any commercial or financial relationships that could be construed as a potential conflict of interest.

The reviewer CG declared a past co-authorship with one of the authors SB to the handling editor.

Copyright © 2020 Alme, Barnaföldi, Barthel, Borshchov, Bodova, van den Brink, Brons, Chaar, Eikeland, Genov, Grimstad, Grøttvik, Helstrup, Herland, Hilde, Keidel, Kobdaj, van der Kolk, Listratenko, Malik, Mehendale, Meric, Nesbø, Odland, Papp, Peitzmann, Pettersen, Piersimoni, Protsenko, Rehman, Richter, Röhrich, Sammøy, Seco, Setterdahl, Shafiee, Skjolddal, Solheim, Songmoolnak, Sudár, Sölje, Tambave, Tymchuk, Ullaland, Underdal, Varga-Köfaragó, Volz, Wagner, Weigold, Widerøe, Xiao, Yang and Yokoyama. This is an open-access article distributed under the terms of the Creative Commons Attribution License (CC BY). The use, distribution or reproduction in other forums is permitted, provided the original author(s) and the copyright owner(s) are credited and that the original publication in this journal is cited, in accordance with accepted academic practice. No use, distribution or reproduction is permitted which does not comply with these terms.